Geodesy constraints on the interior structure and composition of Mars

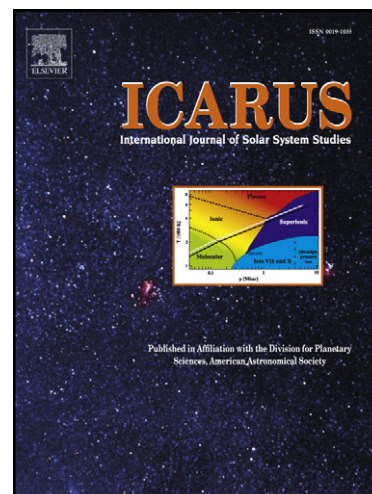A. Rivoldini, T. van Hoolst, O. Verhoeven, A. Mocquet, V. Dehant

Accepted Manuscript

Geodesy constraints on the interior structure and composition of Mars

A. Rivoldini, T. Van Hoolst, O. Verhoeven, A. Mocquet, V. Dehant

Geodesy constraints on the interior structure and composition of Mars

A. Rivoldini[d,e,*], T. Van Hoolst[d], O. Verhoeven[f], A. Mocquet[f], V. Dehant[d]

[a] *Royal Observatory of Belgium, Avenue Circulaire 3, B-1180 Brussels, Belgium*
[b] *Universtité Catholique de Louvain, Earth and Live Institute, Georges Lemaître Centre for Earth and Climate Research*
[c] *Université de Nantes, Nantes Atlantique Universités, CNRS, UMR 6112, Laboratoire de Planétologie et Géodynamique, UFR des Sciences et des Techniques, B.P. 92208, 2 rue de la Houssinière, 44322 Nantes Cedex 3, France*

---

*Corresponding author
Email addresses: Attilio.Rivoldini@oma.be (A. Rivoldini), Tim.VanHoolst@oma.be
(T. Van Hoolst), Olivier.Verhoeven@univ-nantes.fr (O. Verhoeven),
Antoine.Mocquet@univ-nantes.fr (A. Mocquet), Veronique.Dehant@oma.be (V. Dehant)

Geodesy constraints on the interior structure and composition of Mars

A. Rivoldini[d,e,*], T. Van Hoolst[d], O. Verhoeven[f], A. Mocquet[f], V. Dehant[d]

[d]Royal Observatory of Belgium, Avenue Circulaire 3, B-1180 Brussels, Belgium
[e]Universtité Catholique de Louvain, Earth and Live Institute, Georges Lemaître Centre for Earth and Climate Research
[f]Université de Nantes, Nantes Atlantique Universités, CNRS, UMR 6112, Laboratoire de Planétologie et Géodynamique, UFR des Sciences et des Techniques, B.P. 92208, 2 rue de la Houssinière, 44322 Nantes Cedex 3, France

Abstract

Knowledge of the interior structure of Mars is of fundamental importance to the understanding of its past and present state as well as its future evolution. The most prominent interior structure properties are the state of the core, solid or liquid, its radius, and its composition in terms of light elements, the thickness of the mantle, its composition, the presence of a lower mantle, and the density of the crust. In the absence of seismic sounding only geodesy data allow reliable constraining the deep interior of Mars. Those data are the mass, moment of inertia, and tides. They are related to Mars' composition, to its internal mass distribution, and to its deformational response to principally the tidal forcing of the Sun. Here we use the most recent estimates of the moment of inertia and tidal Love number k_2 in order to infer knowledge about the interior structure of the Mars.

We have built precise models of the interior structure of Mars that are parameterized by the crust density and thickness, the volume fractions of upper mantle mineral phases, the bulk mantle iron concentration, and the size and the sulfur concentration of the core. From the bulk mantle iron concentration and

*Corresponding author
Email addresses: Attilio.Rivoldini@oma.be (A. Rivoldini), Tim.VanHoolst@oma.be (T. Van Hoolst), Olivier.Verhoeven@univ-nantes.fr (O. Verhoeven), Antoine.Mocquet@univ-nantes.fr (A. Mocquet), Veronique.Dehant@oma.be (V. Dehant)

from the volume fractions of the upper mantle mineral phases, the depth dependent mineralogy is deduced by using experimentally determined phase diagrams. The thermoelastic properties at each depth inside the mantle are calculated by using equations of state. Since it is difficult to determine the temperature inside the mantle of Mars we here use two end-member temperature profiles that have been deduced from studies dedicated to the thermal evolution of Mars. We calculate the pressure and temperature dependent thermoelastic properties of the core constituents by using equations state and recent data about reference thermoelastic properties of liquid iron, liquid iron-sulfur, and solid iron. To determine the size of a possible inner core we use recent data on the melting temperature of iron-sulfur.

Within our model assumptions the geodesy data imply that Mars has no solid inner core and that the liquid core contains a large fraction of sulfur. The absence of a solid inner is in agreement with the absence of a global magnetic field. We estimate the radius of the core to be 1794 ± 65km and its core sulfur concentration to be 16 ± 2wt%. We also show that it is possible for Mars to have a thin layer of perovskite at the bottom of the mantle if it has a hot mantle temperature. Moreover a chondritic Fe/Si ratio is shown to be consistent with the geodesy data, although significantly different value are also possible. Our results demonstrate that geodesy data alone, even if a mantle temperature is assumed, can almost not constrain the mineralogy of the mantle and the crust. In order to obtain stronger constraints on the mantle mineralogy bulk properties, like a fixed Fe/Si ratio, have to be assumed.

1. Introduction

After more than thirty years of space missions to Mars the wealth of knowledge about the planet Mars has dramatically increased, making it arguably the best-known planet of the solar system after the Earth. However only few observations give reliable constraints on the deep interior of the planet. Among

3

the most prominent are the average density, the mean moment of inertia and the tidal Love number k_2. The average density of $3935 kg/m^3$ is about 37% smaller than the density of Earth. The value of the moment of inertia requires a depth increasing density and the presence of a dense core. The size, state and composition of the core is however only weakly constrained by the value of the moment of inertia. A stronger constraint is provided by the tidal Love number k_2 (Van Hoolst et al., 2003), which indicates that the core is at least partially liquid and in a range of [1520, 1840]km (Yoder et al., 2003). Other relevant constraints to the interior structure are provided by joint inversion of topography and gravity field, leading to estimates of crust thickness and average crust density (e.g. Neumann et al., 2004; Wieczorek and Zuber, 2004).

Knowledge of the chemical composition of Mars has been inferred from cosmochemical considerations, in-situ samples and from analyses of the SNC meteorites. The latter consist of a set of igneous rocks and are widely agreed to originate from Mars (McSween, 1994). If the SNC meteorites are representative of the Martian mantle then it can be concluded that, compared to the Earth, the Martian mantle is richer in FeO (about 18wt% compared to 8wt%, e.g. Robinson and Taylor (2001)), has a higher abundance of moderately volatile elements, and has lower abundances of siderophile elements with chalcophile affinities, indicating that most of the sulfur has segregated to the core (McSween, 1994). Bulk compositional models, which assume that Mars is the parent body of the SNC meteorites, either are based on chemical analysis of the SNC's, supplemented by assumptions relating the mantle composition to the bulk composition (like the assumption of achondritic CI bulk Fe/Si ~ 1.7) (Dreibus and Wänke, 1985), or use ratios of specific isotopes found in the SNC's and match them via mass balance equations to mixtures of different chondritic material (Burbine and O'Brien, 2004). The bulk models of Dreibus and Wänke (1985), Lodders and Fegley (1997), Sanloup et al. (1999), Mohapatra and Murty (2003) differ only by a few percent in mass fractions of chemical compounds CaO, FeO, MgO, Al_2O_3, and SiO_2 (CFMAS), in core mass ratios, and in core light element fractions. The relative differences in the CFMAS elements of the individual models

4

results in notable different volume fractions of the upper mantle mineral modes olivine, pyroxenes and garnet Table [2]. In the above bulk models, the core has a mass weight ratio of about 20%, is principally composed of iron with a lower fraction of nickel ($6 - 8\mathrm{wt}\%$), and is thought to have sulfur as most abundant light element ($10 - 17\mathrm{wt}\%$). This large fraction of sulfur in the core results in a significant depression of the melting temperature of the core material aggregate compared to pure iron (Fei et al., 2000; Stewart et al., 2007) and implies that models based on the above bulk composition most likely have a molten outer core.

Models of the interior structure of Mars assume that the planet is spherical and isotropic. They are constrained by the mass, the mean moment of inertia (e.g. Longhi et al., 1992; Mocquet et al., 1996; Sohl and Spohn, 1997; Zharkov and Gudkova, 1999), and more recently by the tidal Love number k_2 (e.g. van Thienen et al., 2006; Khan and Connolly, 2008; Zharkov et al., 2009). The normalized mean moment of inertia is

$$MOI = \frac{I_a}{m_a r_a^2} = \frac{A + B + C}{3 m_a r_a^2} \tag{1}$$

where m_a, r_a and $A < B < C$ are the mass, the average radius, and the principal moments of inertia. The most recent estimate of the moment of inertia (see Table [1]) has been obtained from a combined analysis of Earth bound tracking of the Mars orbiting satellites MRO, Odyssey and MGS and from the Mars landers Pathfinder and Viking (Konopliv et al., 2011). The tidal Love number k_2 (see Table [1]) has been estimated from satellite tracking data alone (Yoder et al., 2003; Konopliv et al., 2006; Lemoine et al., 2006; Marty et al., 2009; Konopliv et al., 2011).

Interior models of Mars either rely on previously established mantle mineralogy models (e.g. Sohl and Spohn, 1997; van Thienen et al., 2006; Zharkov et al., 2009), or on mantle mineralogies inferred from the data (Khan and Connolly, 2008). The crust is modeled based on the composition of the SNC meteorites

Planetocentric constant	$G\,m_a\ [\mathrm{km}^3\mathrm{s}^{-2}]$	$42828.37440 \pm 0.00028^a$
Mass	$m_a\,[10^{23}\mathrm{kg}]$	6.41855 ± 0.0008^b
Equatorial radius	$r_e\,[\mathrm{km}]$	3396.2 ± 0.1^c
Polar radius	$r_p\,[\mathrm{km}]$	3376.2 ± 0.1^c
Volumetric mean radius	$r_a\,[\mathrm{km}]$	3389.5 ± 0.2^c
Mean density	$\rho_a\,[\mathrm{kg/m}^3]$	3934.97 ± 1.2
Norm. polar moment of inertia	$C/m_a r_e^2$	0.3644 ± 0.0005^a
Norm. mean moment of inertia (MOI)	$I/m_a r_a^2$	0.3645 ± 0.0005^d
Gravitational polar oblateness	$J_2 = -C_{20}$	$1.956607\,10^{-3}$
Elastic tidal Love number	k_2	0.159 ± 0.009^a

Table 1: Physical parameters of Mars. a: Konopliv et al. (2011), b: with $G = (6.67259 \pm 0.00085)\,10^{-11}\mathrm{m}^3\mathrm{s}^{-2}\mathrm{kg}^{-1}$, c: Seidelmann et al. (2002). $MOI = I/m_a r_a^2 = \left(C/m_a r_e^2 - \frac{2}{3}J_2\right)(r_e/r_a)^2$.

(Sohl and Spohn, 1997; Zharkov and Gudkova, 2005), or by assuming a range of values for the crust density and thickness (e.g. van Thienen et al., 2006; Zharkov et al., 2009; Khan and Connolly, 2008). In those models, the mantle temperature profiles are either provided from independent studies dedicated to the thermal evolution of the planet (e.g. Mocquet et al., 1996; van Thienen et al., 2006), calculated by assuming a radial distribution of heat generating radioactive elements and model dependent parameters for heat transport (Sohl and Spohn, 1997), or estimated from the data together with the other parameters of the model (Khan and Connolly, 2008). Finally, in all the models the core is assumed to be made of iron with smaller fractions of light elements. In order for the models to fit the planet's mass and average moment of inertia the parameters characterizing the crust and mantle are adjusted together with the core size and fractions of light elements inside the core.

Here, we will not assume a bulk composition of Mars but rather parameterize the mantle mineralogy in terms of the mantle iron number (Fe#) and volume fractions of the low pressure mineral phases olivine, orthopyroxene, Ca-pyroxene, and garnet (see Sec. 2). The other parameters of our models are the crust density and thickness, the composition of the core and its radius. In Secs. 3 we state the mathematical relations between the model parameters and the geodesy observables. Since those relations are highly non linear and since the number of parameters is notably larger than the number of data we use a

6

Bayesian inversion method to infer knowledge on the parameters of the interior structure model (the method is presented in Sec. 4). For two end-member mantle temperature profiles, we then first present the results obtained from the inversion of Mars' mean density and moment of inertia (see Sec. 5.1). Then in a second step, Sec. 5.2, we impose the value of the tidal Love number k_2 and show how this supplemental datum leads to a more concise knowledge on the model parameters. In particular, we demonstrate that geodetic constraints can significantly improve our understanding of the core of Mars. Next, we compare our solutions with established bulk models and investigate if within the set of compatible models the pressure and temperature conditions at the bottom of the mantle allow for a perovskite layer. Finally, we discuss how an assumed bulk chondritic Fe/Si ratio, given mantle mineralogy models, or an assumed core composition constrains our knowledge on the remaining parameters of the interior structure model.

2. Composition modeling

2.0.1. Crust

The crust of Mars has a complicated regional and global structure but to first order it is essentially dichotomic. We will, however, not include the crust dichotomy in our models of the interior structure since its effect on the geodesy observables is well below their uncertainty. The difference in moment of inertia of Mars between a model with a degree-one crust dichotomy and an otherwise similar model with a spherically symmetric crust is at least an order of magnitude smaller than the uncertainty on the moment of inertia, and the effect of a crust dichotomy on the Love number k_2 can also be neglected. For our interior structure model we will therefore assume that the crust is a uniform spherical shell that is determined by only two parameters: the average crust density and crust thickness. Estimates of the average crust thickness and crust density can be estimated by inverting topography and gravity data. Recent estimates on Mars' crust thickness and density can for instance be found in Wieczorek and

7

Zuber (2004). The average crustal thickness is estimated to lie within an interval of $38 - 62$km if the crust density is within $2700 - 3100$kg/m^3. Here, for our calculations we use somewhat broader intervals: $30 - 80$km for the crust thickness and $2700 - 3200$kg/m^3 for the crust density. For all models the P and S seismic velocities are set to 7900m/s and 4550m/s.

2.0.2. Mantle

In our models the bulk mantle composition is uniquely determined by five parameters: the bulk Fe# number and the volume fractions of the low pressure mineral phases olivine, orthopyroxene, Ca-pyroxene, and garnet. For given values of those parameters and by using high pressure and temperature phase diagrams the volume fractions of the resulting high pressure phases can be determined at each (P, T) by considering two independent subsystems (Vacher et al., 1998; Verhoeven et al., 2005). The first subsystem is determined by the phase diagram of olivine and its high pressure phases, ringwoodite, wadsleyite, Mg-wüstite, and perovskite, the second subsystem is governed by the phase diagram of pyroxene-garnet and their high pressure phases garnet, akimotoite and perovskite. The depths where the transition to the higher pressure phases occur depend on temperature, pressure, and on the depth dependent mantle iron content. The iron content variations with depth inside the mantle of Mars are unknown, although, they are relatively small in the deep mantle of Earth (e.g. Verhoeven et al., 2009). We therefore here assume that the mantle iron concentration is constant. Since, compared to the mantle of Earth, Mars mantle models based on SNC meteorites indicate that Mars is depleted in aluminum and calcium (see Table [2]) and following Verhoeven et al. (2005) we neglect aluminum bearing mineral phases and expected small fractions of Ca-bearing garnet in our calculations. The chemical formulas of the mantle mineral phases that we use for the thermoelastic calculations are listed in Table [B.13].

For our study of the constraints imposed by geodesy data on the interior of Mars, we consider two settings. First, we only use weak prior knowledge on the mantle mineralogy parameters: the volume fractions of olivine, orthopyroxene,

8

	DW84	LF97	EH45	EH70	MM03
Bulk mantle composition (wt%) *in major oxides*					
CaO	2.4	2.4	2.0	2.0	1.9
FeO	17.9	17.2	17.7	11.4	16.9
MgO	30.1	29.7	27.3	27.3	29.1
Al_2O_3	2.9	2.9	2.5	2.5	2.5
SiO_2	44.4	45.4	47.5	51.0	47.1
*Mineral modes (*vol%*)*					
olivine	58.7	42.5	25.5	4.1	33.4
orthopyroxene	20.6	42.9	61.2	81.4	54.5
Ca-pyroxene	11.4	3.1	3.1	2.1	2.1
garnet	9.3	11.5	10.2	12.4	10.0
Fe#	25	24	28	20	24

Table 2: Bulk mantle composition in weight fractions of major oxides and volume fraction of mantle mineral modes. DW84 Dreibus and Wänke (1985), LF97 Lodders and Fegley (1997), EH45 and EH70 Sanloup et al. (1999), and MM03 Mohapatra and Murty (2003).

and garnet are allowed to vary in a $0 - 100$vol% range, that of Ca-pyroxene in a $0 - 50$vol% range and the Fe# number is chosen in a $10 - 45\%$ range. Those parameters are part of the larger parameter set of the interior structure model, which we try to constrain by the geodetic measurements. Secondly, we use the mantles of the models Dreibus and Wänke, Lodders and Fegley and Mohapatra and Murty (referred to as DW84, LF97, and MMO3) and the two mantle mineralogies of the models of Sanloup et al. (referred to as EH45 and EH70) and determine the constraints that the geodetic measurements provide on the remaining parameters of the interior structure for those choices of mantle mineralogies.

9

2.0.3. Core

The core of Mars is thought to be made mainly of iron with an unknown smaller fraction of nickel and other light elements. From the chemical affinity of light elements to iron-nickel mixtures, the possible light elements are S, Si, O, C, H, P,.. in binary, ternary or more complicated systems with Fe and Ni. The identities and amounts of the light elements found in the iron dominated core depend on the chemical composition of the materials that accreted to form the planet and on the temperature and pressure during core formation. However, those unknowns can only be roughly estimated as they strongly depend on the proposed planetary and core formation scenario. Only in-situ analyses of rock samples representative of the bulk composition of Mars do allow to further constrain the composition of the core, although they remain dependent on core formation scenarios and mantle core chemical equilibration hypotheses. Presently, the only rock samples widely admitted to be of Martian origin are the SNC meteorites. The analysis of the SNC's indicate that iron, nickel and the light element sulfur are the principal constituents of the core. Additional evidence for the presence of sulfur comes from the fact that it has been found in many nickel-iron-meteorites under the form of FeS. Of all the light elements, sulfur and silicon are most easily incorporated into planetary cores of terrestrial planets as their solubility in molten iron is high over an extended pressure range (Poirier, 1994). In contrast, for example oxygen solubility in liquid iron is below 1wt% at ambient pressure and, although increasing with increasing pressure, remains small and below about 1wt% for pressures below 10GPa (Tsuno et al., 2007), relevant for the core formation of Mars.

In ternary iron systems, the solubility of light elements is more complicated. For example, Si does not dissolve into liquid $Fe - S$ at ambient pressure, the first melt to percolate through the silicate matrix during core formation, since at that pressure the $Fe - S - Si$ system exhibits a large region of immiscibility in a temperature composition representation. This miscibility gap only closes at about 14GPa (Sanloup and Fei, 2004). Since the differentiation of Mars took

place at pressures that are lower than about 20GPa (about the pressure at the core mantle boundary), small amounts of Si could have dissolved in the $Fe - S$ melt, but it is unlikely that significant amounts of Si were incorporated into the core during core formation. Oxygen, although almost immiscible with liquid iron at low pressure, could be dissolved in $Fe - S$ melts since the miscibility increases with increasing temperature, pressure and sulfur weight fraction (Tsuno et al., 2007). However, data in Tsuno et al. (2007) and Rubie et al. (2004) suggest that at the low pressures characteristic for Mars' differentiation and for the sulfur concentration considered here ($x_S < 22$wt%) oxygen too can only be present in small amounts in Mars' core.

As a consequence of the planet's cooling history, a solid inner core may have formed in the initial liquid core of Mars. Light elements are not only dissolved in the liquid $Fe - Ni$ outer core mixture but can also be incorporated in the solid $Fe - Ni$ inner core alloy. The solubility of Si in solid Fe is nearly identical to its solubility in liquid Fe (Kuwayama and Hirose, 2004), whereas S only dissolves for less than about 1wt% in solid Fe at the low core pressures in Mars (Li et al., 2001). The solubility of S in solid $Fe - Ni$ (Zhang and Fei, 2008) increases to more than 2wt% depending on the amount of Ni. The light elements S and Si also have the important property that they lower the melting temperature of the iron system with respect to pure iron, contrary to oxygen which does not significantly depress the melting temperature of Fe (Boehler, 1992; Tsuno et al., 2007). For example, at 21GPa the melting temperature of Fe decreases by about 60K for each additional weight percent of S (Fei et al., 2000) and the temperature decrease for the inclusion of Si is about 10K (Kuwayama and Hirose, 2004). Note that the melting temperature decreases with increasing amounts of nickel (Stewart et al., 2007; Zhang and Fei, 2008) (for about 8wt% of Ni at 23GPa the melting temperature decrease is about 30K).

The above data for binary and ternary iron systems suggest that it is unlikely that Mars' core contains significant amounts of light elements other than sulfur. Moreover, in order to justify the observed liquid outer core of Mars (Yoder et al., 2003), sulfur is a strong candidate as among all the considered light

11

elements, already small amounts allow for strong temperature depression of the melting temperature of the iron-rich core material. On the basis of the above arguments we therefore here neglect the effect of other light elements beside sulfur on the thermoelastic properties of the core material. We also neglect Ni, which is likely present up to 10wt% inside the core. Its thermoelastic properties are close enough to those of iron to not significantly affect the core density and compressibility at those concentrations.

Solid phases start to crystalize out of the liquid core solution when the local temperature drops below the local liquidus temperature. At pressures relevant for the core of Mars, the solid is mostly pure $\gamma - Fe$ if the sulfur concentration is smaller then the eutectic concentration (left of the eutectic) and consists of iron-rich iron-sulfur compounds (Fe_2S, $Fe_{3+x}S_2$, Fe_3S) if the sulfur concentration is larger than the eutectic concentration (right side of the eutectic) (Fei et al., 2000). At the typical pressures inside Mars' core (about $18 - 40$GPa, see Sec.5) and for sulfur concentrations to the left of the eutectic the iron rich solid phase either starts to solidify first at the center of the planet or at the core mantle boundary depending on the sulfur fraction of the solution (Stewart et al., 2007). In the first case, a solid inner core starts to crystalize from the center of the planet outwards and in the second case the iron rich solid precipitates from the core mantle boundary towards the center if upon down-falling the local temperature is below the solidus. With ongoing iron solidification the outer core's liquid sulfur concentration gradually increases until it reaches the eutectic concentration. Upon further cooling, the outer core liquid gradually freezes, and solids of eutectic composition are deposited onto the solid inner core. On the other hand if the initial core sulfur weight fraction is to the right of the eutectic, solid iron-rich iron-sulfur compounds will crystallize out of the liquid where the local temperature drops below the liquidus. Depending on the pressure and temperature conditions, this iron-rich iron-sulfur compounds will either result in a growing inner core or a deposition of a light element rich layer at the core-mantle boundary (Hauck et al., 2006). The S fraction in the remaining liquid will gradually decrease until the eutectic concentration is reached and the core

12

liquid gradually freezes out upon further cooling.

In order to build consistent models of the core of Mars, the melting temperature has to be known precisely over a large range of pressures (from about 15GPa to about 50GPa) and sulfur concentrations. Unlike the melting temperature of pure $\gamma - $Fe (e.g. Boehler, 1993; Shen et al., 1998) and to a lesser extent the melting temperature at the eutectic concentration (e.g. Fei et al., 2000; Li et al., 2001; Stewart et al., 2007; Chudinovskikh and Boehler, 2007; Chen et al., 2008; Morard et al., 2008; Andrault et al., 2009), melting temperatures of the Fe $-$ S systems for intermediary sulfur concentrations have only been measured at a few discrete pressures and for a small set of sulfur concentrations (e.g. Fei et al., 2000; Li et al., 2001; Stewart et al., 2007; Andrault et al., 2009). We therefore use an empirical expression for the core melting law for sulfur concentrations that are smaller or equal to the sulfur concentration at the eutectic. For lack of data we assume that at a given pressure the melting temperature decreases linearly with the sulfur concentration from the melting temperature of pure $\gamma - $Fe to the temperature of the eutectic concentration. The pressure dependence of the melting temperature is then induced from the pressure dependent melting temperature of $\gamma - $Fe and from the pressure dependent temperature of the eutectic concentration. The melting temperature as a function of pressure can then be written as

$$T_m(P, x_\text{S}) = T_{m,\text{Fe}} - \frac{T_{m,\text{Fe}}(P) - T_e(P)}{x_e(P)} x_\text{S}, \tag{2}$$

where $T_{m,\text{Fe}}(P)$ is the melting temperature of $\gamma - $Fe, and $T_e(P)$ and $x_e(P)$ the eutectic temperature and the eutectic sulfur concentration.

In order to obtain a parameterization of the melting temperature of $\gamma - $Fe as a function of pressure we fit a cubic polynomial to the melting data of Boehler (1993) and Shen et al. (1998) over the $[5, 60]$ GPa pressure range:

$$T_{m,\text{Fe}}(P) = T_{0,\text{Fe}} + a_1 P + a_2 P^2 + a_3 P^3. \tag{3}$$

The values of the parameters a_1, a_2, and a_3 are given in Table [3]. Fig.[1] shows the parameterized iron melting temperature together with the used iron melting

13
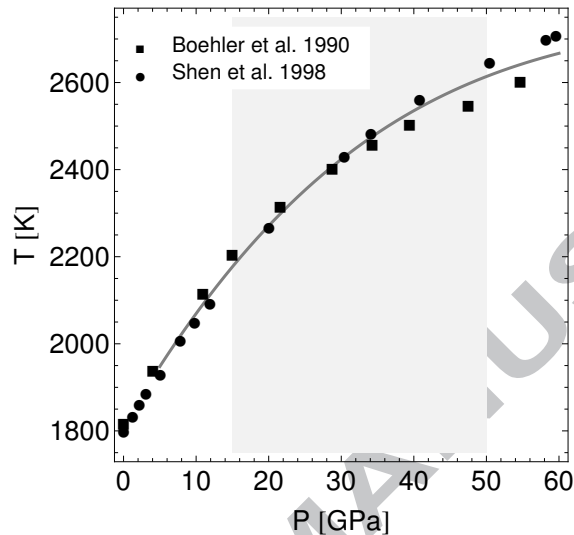
data.

Figure 1: $\gamma -$ Fe melting temperature as a function of pressure. The melting data are from Boehler (1993) and Shen et al. (1998). The gray shaded domain represents the pressure range inside the core of Mars if $r_{\mathrm{cmb}} \leq 2200$km.

Measured melting temperatures at the eutectic concentration for different pressures are shown in Fig.[2a]. At low pressures the eutectic melting temperature decreases with increasing pressure and reaches a minimum near 14GPa, the pressure of formation of the intermediate compound Fe_3S_2. For pressures larger than 14GPa the eutectic melting temperature increases with increasing pressure with an inflection point at about 21GPa, the pressure of formation of the intermediate compound Fe_3S. To obtain an expression for the temperature at the eutectic concentration as a function of pressure we independently fit the low pressure data, 3GPa $\leq P \leq 14$GPa, and the high pressure data, 21GPa $\leq P < 60$GPa, to two linear functions in P. The eutectic melting temperature over the intermediary pressure range, 14GPa $\leq P < 21$GPa, is then obtained by joining the eutectic temperatures at 14GPa from the first fit to the

14

eutectic temperatures at 21GPa of the second fit by a third linear function in P. The parameterized from of the eutectic melting temperature T_e as a function of pressure is then given as

$$T_e(P) = T_{e,0} + b_1(P - P_{e,0}) \tag{4}$$

in the three pressure intervals, with parameter values given in Table [4]. The resulting empirical melting temperature at the eutectic concentration together with the used data are shown in Fig.[2a].

The sulfur concentration at the eutectic melting temperature decreases with increasing pressure and appears to asymptotically reach a fixed value of about 0.12 at high pressure (see Fig.[2b]). The experimental data can be adequately described by an exponentially decreasing function with pressure:

$$x_e(P) = x_{e,\infty} + c_1 e^{-c_2 P}, \tag{5}$$

where the numerical values of the parameters $x_{e,\infty}$, c_1, and c_2 are given in Table [3]. Fig.[2b] shows the fit adequately describes the data used.

Our modeled melting temperatures of Fe $-$ S for different fractions of sulfur are shown in Fig.[3] as a function of pressure together with two typical core adiabatic temperature profiles and the melting temperature at the eutectic concentration. In our parametrization the slope of the melting temperature is less steep than the slope of the adiabatic temperature profile for sulfur concentrations smaller than about 0.5wt% and upon cooling a solid inner core crystallizes from the center outward. For sulfur concentrations larger than 0.5wt% the slope of the melting temperature is steeper than the adiabatic temperature profile and solid iron is expelled from the Fe $-$ S solution at the top of the core and precipitates towards the center of the core to form an inner core. At sulfur concentrations of about 0.5wt% the melting curve and the adiabatic temperature profile can intersect simultaneously at the center, the top of the core, and at intermediary locations. An inner core than forms from crystallizing iron at the center of the core and from precipitating solid iron. Since upon inner core growth the liquid outer core's sulfur concentration increases, the location where

15
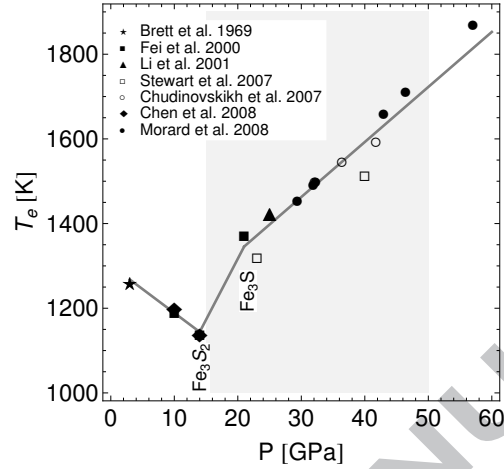
(a)
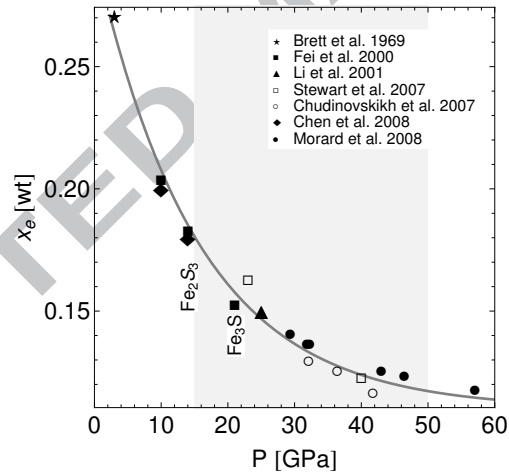
(b)

Figure 2: Eutectic temperature as a function of pressure (a) and eutectic sulfur concentration as a function of pressure (b). The data about the eutectic temperature and sulfur concentration are from Brett and Bell (1969), Fei et al. (2000), Li et al. (2001), Stewart et al. (2007), Chudinovskikh and Boehler (2007), Chen et al. (2008), and Morard et al. (2008). The gray shaded domain represents the pressure range inside the core of Mars if $r_{\mathrm{cmb}} \leq 2200\mathrm{km}$.

16

the core temperature is lower than the melting temperature can shift from the bottom of the core towards the top of the core. However, we only consider the case where the inner core forms from solid iron precipitating from the top of the core since in our parametrization the other scenarios only occur at very low sulfur concentrations.

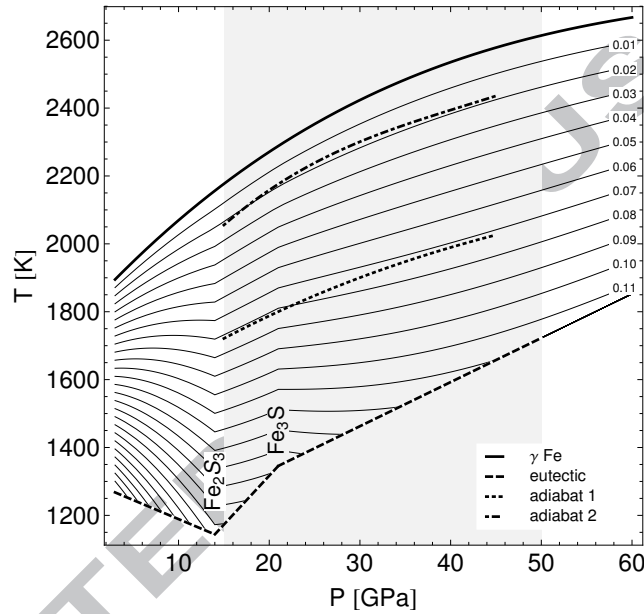Figure 3: Fe − S melting temperature as a function of pressure for different fractions of sulfur. The black curve is the melting temperature of $\gamma -$ Fe, the dashed curve is the melting temperature at the eutectic concentration, the dotted and dash-dotted curves correspond to two Mars core adiabatic temperature profiles. The gray shaded domain represents the pressure range inside the core of Mars if $r_{\rm cmb} \leq 2200$km.

$T_{0,\mathrm{Fe}}$ [K]	1811
a_1 [K/GPa]	-0.32
a_2 [K/GPa^2]	28.95
a_3 [K/GPa^3]	0.0013
$x_{e,\infty}$	0.11
c_1	0.187
c_2 [GPa^{-1}]	-0.065

Table 3: Parameter values for empirical iron melting temperature as a function of pressure $T_{m,\mathrm{Fe}}$ and eutectic sulfur concentration x_e as a function of pressure.

	$3\,\mathrm{GPa} \leq P < 14\,\mathrm{GPa}$	$14\,\mathrm{GPa} \leq P < 21\,\mathrm{GPa}$	$21\,\mathrm{GPa} \leq P < 60\,\mathrm{GPa}$
$P_{e,0}$ [GPa]	3.	14.	21.
$T_{e,0}$ [K]	1268.	1144.	1255.
b_1 [K/GPa]	$-11.$	29.	13.

Table 4: Parameter values for empirical eutectic temperature T_e as a function of pressure.

3. Interior structure

3.1. Structural equations

We construct spherically symmetric models of the interior structure of Mars in which interior structure quantities only depend on the radial distance to the center r. We assume Mars to be in hydrostatic equilibrium:

$$\frac{dP}{dr} = -\rho g. \tag{6}$$

Here, P is pressure, ρ mass density and g gravity. The models also satisfy Poisson's equation

$$\frac{dg}{dr} = 4\pi \mathrm{G}\rho - 2\frac{g}{r}, \tag{7}$$

where G is the universal gravitational constant. Both equations depend on the density ρ, which we calculate from an equation of state (EoS) specifying the dependence of the density on pressure, temperature and composition (see Appendix A and Appendix B)

The temperature profile can be calculated by assuming that Mars is in thermal equilibrium and by specifying at each location the primary method of energy

18

transfer. Thermal equilibrium is the balance between the energy lost by outward energy flux and the internal energy generation and can be expressed as

$$\frac{dq}{dr} = \rho\epsilon - 2\frac{q}{r},$$

(8)

where q is the outward heat flux per unit area and unit of time and ϵ the specific heat production rate. If energy is transported mainly by convection, the temperature gradient can be approximated by the adiabatic temperature gradient (e.g. Stacey, 1977)

$$\frac{dT}{dr} = -\frac{\gamma}{K_S}\rho g T,$$

(9)

where $\gamma = \alpha K_S/\rho c_P$ is the thermodynamic Grüneisen parameter, c_P the specific heat at constant pressure, α the thermal expansion coefficient, and K_S the adiabatic bulk modulus. For conduction, the thermal gradient is given by

$$\frac{dT}{dr} = -\frac{q}{k},$$

(10)

where k is the thermal conductivity.

3.2. Mantle and crust

The temperature is difficult to determine because it depends on the thermal history of Mars, the unknown amount of radio-active elements in the core, mantle, and crust and the fraction of light elements in the core. Therefore, we here do not solve differential Eqs. (8) and (9) (or (10)) for the thermal quantities q and T in the mantle, but use instead published mantle temperature profiles from studies dedicated to the thermal evolution of Mars. We consider two temperature profiles (Verhoeven et al., 2005), a hot and a cold end-member. Both temperature profiles have been devised under the premise that Mars is a one-plate planet undergoing stagnant lid convection. They are plausible end members suggested by results of models designed for Mars thermal evolution (Breuer and Spohn, 2003). The thermal profiles have been constructed under the assumptions of an early episode of geomagnetic activity (during the first 500 million years) and of a crust growth history in agreement with the present

19

day average crustal thickness of $50 - 120$km. The hot profile has been obtained by assuming a thermal conductivity of $2W/mK$ in the crustal basaltic layer and a larger value of $4W/mK$ for the rest of the mantle. For the cold temperature profile a thermal conductivity of $4W/mK$ has been used everywhere. Note that from the results of Takahashi (1990) on the liquidus and solidus of anhydrous peridotite it follows that the cold temperature profile never crosses the solidus and that the hot temperature profile would allow for a small fraction of partial melt at the bottom of the lithosphere. We will not take into account this small fraction of melt in our modeling of the interior structure since it will only result in negligible changes in the density and elastic moduli.

Both temperature profiles have been established for a specific interior structure (e.g. given core size), but we use them for the mantles of all the interior structure models. In practice, the temperature profiles are adapted to a given mantle depth by shortening or lengthening their adiabatic part and leaving the other parts unchanged.

Compared to other published temperature profiles, our cold end-member is very similar to the mantle temperature profile proposed by Sohl and Spohn (1997) for their model B, whereas our hot end-member is comparable to the temperature profiles suggested by Zharkov and Gudkova (2005) and Khan and Connolly (2008) for depths deeper than 1000km but hotter for shallower depths. Note that the temperature profiles of Sohl and Spohn (1997) and Zharkov and Gudkova (2005) have been established by assuming a distribution of radioactive elements in the mantle and heat flow at the core mantle boundary or at the surface. On the other hand, the temperature profile of Khan and Connolly (2008) has been inferred from a joint inversion of geodesy data (mass, MOI, and Love number k_2). We decided not to estimate the mantle temperature from the data since there is a strong correlation between mantle composition, particularly iron concentration, and mantle temperature. Those correlations cannot be disentangled by using as data integrated global quantities like the moment of inertia and the Love number k_2. Even if the mantle density and P- and S-wave data were known as a function of depth the ambiguities between mantle compo-

sition and temperature cannot be resolved (e.g. Matas et al., 2007). In order to estimate the mantle temperature and composition additional independent observables, like the mantle electrical conductivity, are necessary (e.g. Verhoeven et al., 2009).

The mantle model can then be determined as follows. Assuming a given crust thickness, a constant average crust density, a mantle temperature profile, and a mantle composition expressed in volume fractions of the low pressure mineral phases, olivine (ol), orthopyroxene (opx), Ca-pyroxene (cpx), and garnet (gt), together with a value of the iron number (Fe#), we first integrate Eqs. (6) and (7) from the surface to the bottom of the crust, starting from the boundary conditions at the surface $r = r_a$

$$P(r_a) = 0, \tag{11}$$

$$g(r_a) = \frac{Gm_a}{r_a^2}. \tag{12}$$

The resulting pressure and gravity at the mantle-crust boundary are the boundary conditions to integrate Eqs. (6) and (7) from the bottom of the crust to the core-mantle boundary. These equations have to be supplemented with phase diagrams and equations of state to include pressure-induced compression and thermal expansion effects on the thermoelastic properties, as explained in Appendix B.

3.3. Core

The primary mechanism of present heat transport in the core of Mars is uncertain. However, spacecraft data about crustal magnetizations (Acuña et al., 1999) suggest that Mars once had a global magnetic field and therefore a core dynamo in its early history. The high thermal conductivity of the core material and the absence of a global magnetic field, which would require core convection (e.g. Stevenson, 2001), suggest that the present heat transport in the core is by conduction. Since the parameters governing the conductive heat transport are not well known, the core temperature is rather uncertain, although intermediary to an isotherm and adiabat. We have calculated Mars models and observable

21

geodesy quantities for both end-member core temperature profiles. However, since the differences in calculated geodesy quantities between adiabatic and isothermal core temperature profile are significantly smaller than the measured uncertainties we here only present results for models with an adiabatic core temperature both in the liquid outer core and solid inner core (if present).

We calculate the temperature profile in the core, given the temperature at the core-mantle boundary, by assuming that both the liquid core and the solid inner core (if present) are convecting. Moreover, we assume that there are no radioactive elements in the core and therefore according to (8) the energy flux through a spherical surface $(4\pi r^2 q)$ is constant in the core.

The three governing equations related to the structure of the core are then given by (6), (7), and (9) for P, g, and T. At the center, we have the initial condition

$$g(0) = 0. \tag{13}$$

At the core-mantle boundary, the three quantities P, g, and T must be continuous.

If an inner core is present one has

$$T_{\mathrm{cmb}} = T_m(P_{\mathrm{cmb}}, x_S^{\mathrm{OC}}). \tag{14}$$

Here, the dependence of the melting temperature on the composition of the outer core (or sulfur weight fraction x_S^{OC} in the outer core) and the pressure have been made explicitly. The three quantities P, g, and T have to be continuous at the inner core boundary (icb) radius r_{icb}.

For a given core size, we integrate 6 differential equations: 3 in the outer core from the core-mantle boundary down and 3 in the solid inner core from the center to the core-mantle boundary. The resulting 6 independent differential equations give rise to 6 integration constants. Since we also solve for the outer-core sulfur weight fraction and the location of the boundary between the inner core and the outer core (icb), we have 8 parameters. These can be determined from 8 conditions: 3 boundary (or continuity) conditions at the cmb, 1 initial

22

condition at the center, 3 continuity conditions at the icb, and the melting temperature at the cmb.

3.4. Mass and moment of inertia

Once the equations for the structure of Mars are solved, the density profile in the whole planet is known. The resulting mass and moment of inertia of spherical volumes with radius r are then calculated from

$$m_a = 4\pi \int_0^{r_a} dr \ \rho(r)r^2, \tag{15}$$

$$I = \frac{8}{3}\pi \int_0^{r_a} dr \ \rho(r)r^4. \tag{16}$$

3.5. Tides

The tides on Mars are mainly the result of the gravitational attraction of the Sun and to a lesser extent of the natural satellites Phobos and Deimos. The magnitudes of the body tides are larger the closer and more massive the tide generating body. Moreover, the response of a tidally forced planet increases with its size, as a result, for the same tide generating potential, tides on larger planets are greater. Therefore, compared to the Earth and to Mercury the body tides on Mars are relatively small. The radial tidal displacement on Mars is about 1 cm (Van Hoolst et al., 2003) whereas for Earth it is about 40 cm and it is expected to be of the order of 1 m on Mercury (Van Hoolst and Jacobs, 2003). Although small, external gravity potential variations resulting from tidally driven mass redistributions inside the planet are nevertheless large enough to be precisely determined by tracking spacecraft orbiting Mars (e.g. Konopliv et al., 2011).

Since Mars is not a perfect elastic body, its deformational response is slightly delayed compared to the tidal forcing exerted by the Sun and by Phobos and Deimos. In particular, the direction between the bulge raised by Phobos on the surface of Mars and the Mars-Phobos direction are not equal. As a result Phobos experiences a secular orbital acceleration. By measuring the orbital change of Phobos the dissipation inside Mars, at the period of the tidal forcing, can be determined (Lainey et al., 2007) and its rheology constrained. Compared to

23

the elastic setting, the Love number k_2 for a non-elastic Mars model is complex and frequency dependent. However, for non-elastic interior models that are compatible with the measured dissipation, the real part of k_2 and the k_2 value of an equivalent elastic model are only negligibly different. Therefore, we here consider only elastic interior models.

The calculations of the deformations and potential variation resulting from the forcing of the tidal potential can be made within the framework of the linear theory of elastic free seismic oscillations (e.g. Dahlen and Tromp, 1998) extended to forced motions (e.g. Rivoldini et al., 2009). The tides of our Mars models are calculated by numerically integrating the ordinary differential equations describing the deformations and external potential variations by using the depth-dependent profiles of density, adiabatic bulk modulus K_S, and shear modulus μ.

The response of a planet to tidal forcing is strongly dependent on its interior structure, especially on the state of the core. A planet with a liquid part is more easily deformable than one that is completely solid and therefore produces a larger response to a tidal forcing. If Mars had a solid core its k_2 value would be smaller than 0.08. Since measured k_2 values are larger than 0.11 (see Table [5]) it can been concluded that core of Mars contains an appreciable liquid part (Yoder et al., 2003). Here we will show that together with the moment of inertia, the k_2 value allows to give a relatively tight constraint on the size of the core.

	k_2
Yoder et al. (2003)	0.145 ± 0.017
Konopliv et al. (2006)	$0.148^* \pm 0.009$
Lemoine et al. (2006)	0.176 ± 0.041
Marty et al. (2009)	0.12 ± 0.004
Smith et al. (2009)	0.236 ± 0.058
Konopliv et al. (2011)	$0.159^* \pm 0.009$

Table 5: Tidal Love numbers k_2 of different authors. k_2 values that have a "*" superscript elastic are corrected for solid tidal friction, atmospheric tide, and inelastic softening.

A sample of recently determined k_2 numbers are given in Table [5]. With

24

the exception of the value of Marty et al. (2009), the k_2 values have overlapping error-bars at the 1σ level. To constrain the interior structure of Mars, we adopt the most recent determination of the k_2 value of Konopliv et al. (2011), who used the most complete model of the spacecraft orbital motion including the effect of atmospheric dust.

4. Method

By using the moment of inertia and the Love number k_2 as geodetic data $\mathbf{D}$, we intend to constrain the following interior structure parameters $\mathbf{X}$: core size, crust density and thickness, and the parameters specifying the mineralogy of the mantle, i.e., the volume fractions of olivine, orthopyroxene, Ca-pyroxene, and garnet and the iron number Fe# . Since the number of parameters (8) is larger than the number of data (2), and since the data have associated uncertainties, we cannot obtain unique solutions for the parameters. Nevertheless for each parameter a range of values that are consistent with the data can be determined. An appropriate method for inferring knowledge about the parameters for this setting is Bayesian inversion (e.g. Tarantola, 2005). Within the Bayesian inversion method, the data and their associated uncertainties are represented by a probability distribution, the data likelihood, which is related to the parameter values by the equations describing the interior structure model. Existing knowledge on the parameters and supplemental modeling assumptions related to the parameters are taken into account by means of a prior, which is a probability distribution on the parameters. From the likelihood and from the prior distribution we then calculate the probability distribution on the parameters given the data.

We assume that the knowledge on the measured moment of inertia and on the tidal Love number are independent and that each datum can be represented by a normal distribution. The probability density function for measuring the data D given the parameters X, the likelihood function, is then written as

$$\mathcal{L}(\mathbf{D}|\mathbf{X}) = \frac{1}{2\pi\sigma_I\sigma_{k_2}} \exp\left\{-\frac{(I(\mathrm{X}) - I^*)^2}{2\sigma_I^2} - \frac{(k_2(\mathrm{X}) - k_2^*)^2}{2\sigma_{k_2}^2}\right\}, \qquad (17)$$

25

where I^* and k_2^* are the measured moment of inertia and Love number and σ_I and σ_{k_2} the associated uncertainties (see Table [1]).

The model parameters $r_{\rm cmb}$, $d_{\rm crust}$, $\rho_{\rm crust}$, Fe#, and the four mantle mineralogy parameters $(X_{\rm ol}, X_{\rm opx}, X_{\rm cpx}, X_{\rm gt})$ are assumed to be independent of each other so that we can write the prior probability density function as

$$\Pi(\mathbf{X}) = \Pi(r_{\rm cmb})\Pi(d_{\rm crust})\Pi(\rho_{\rm crust})\Pi({\rm Fe\#}) \tag{18}$$

$$\Pi(X_{\rm ol}, X_{\rm opx}, X_{\rm cpx}, X_{\rm gt}), \tag{19}$$

where the parameters $r_{\rm cmb}$, $d_{\rm crust}$, $\rho_{\rm crust}$, and Fe# each have a uniform probability distribution and where the probability distribution representing the volume fractions of $X_{\rm ol}$, $X_{\rm opx}$, $X_{\rm cpx}$, and $X_{\rm gt}$ is characterized by the constraint:

$$X_{\rm ol} + X_{\rm opx} + X_{\rm cpx} + X_{\rm gt} = 1 \tag{20}$$

with $X_{\rm ol}$, $X_{\rm opx}$, $X_{\rm gt} \leq 1$ and $X_{\rm cpx} \leq 0.5$ (see Sec. 2.0.2). The marginal prior distributions for ol, opx, cpx, and gt are shown in Fig.[4].
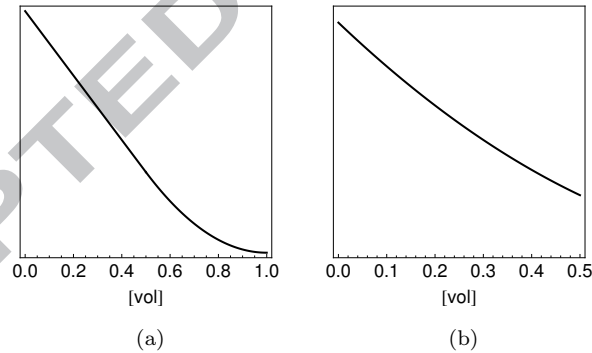
Figure 4: Marginal prior probability density functions for olivine, orthopyroxene, and garnet (a) and Ca-pyroxene (b).

The prior range for the core size $(1000 - 2200{\rm km})$ is chosen such that it allows for interior models with pure solid iron cores and for cores that contain up to 25wt% of sulfur. The prior ranges for the crust density $(2700 - 3100{\rm kg/m^3})$ and crust thickness $(30 - 90{\rm km})$ correspond to the estimates of Wieczorek and

26

Zuber (2004). From the prior probability distribution on $(X_{\mathrm{ol}}, X_{\mathrm{opx}}, X_{\mathrm{cpx}}, X_{\mathrm{gt}})$ and Fe# the corresponding mantle bulk chemical composition can be calculated in terms of weight fractions of CaO, FeO, MgO, and SiO$_2$ by using the chemical formulas of the mineral phases olivine, orthopyroxene, Ca-pyroxene, and garnet (see Fig.[5]). The resulting set of weight fractions of oxides comprise and extend values of proposed Mars mantle models, presumed values of the Earth mantle, and of other terrestrial planets (Khan and Connolly, 2008). The range of each model parameter is given in Table [6].

Figure 5: Probability density functions of mass fractions of CaO (a), FeO (b), MgO (c), and SiO$_2$ (d).

From the likelihood function and from the prior distribution we obtain the posterior probability density function, the joint probability density function for

27

the parameters given the data according to

$$P(\mathbf{X}|\mathbf{D}) = c \, \mathcal{L}(\mathbf{D}|\mathbf{X}) \, \Pi(\mathbf{X}), \tag{21}$$

where the normalization constant c is defined such that

$$\int_{-\infty}^{\infty} d\mathbf{X} \, P(\mathbf{X}|\mathbf{D}) \equiv 1. \tag{22}$$
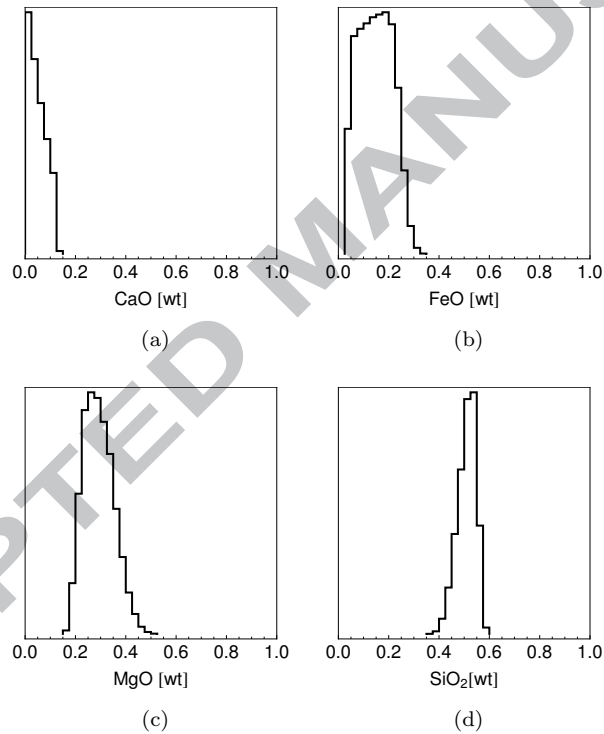
We simulate $P(\mathbf{X}|\mathbf{D})$ with the Metropolis Hastings sampler (Hastings, 1970), which does not require the knowledge of c. The Metropolis Hastings algorithm generates samples from $P(\mathbf{X}|\mathbf{D})$ that we summarize in the next section as (1) histograms, i.e., empirical distributions, (2) median values, and (3) 0.68, 0.95, and 0.997 probability intervals. For convenience those intervals are also denoted as 1σ, 2σ, and 3σ. We estimate the probability intervals as the narrowest intervals $[a, b]$ such that

$$\int_{a}^{b} d\mathbf{X} \, P(\mathbf{X}) = P([a, b]) \tag{23}$$

and $P([a, b])$ is 0.682, 0.954, or 0.997. Note that for the prior distribution on olivine, orthopyroxene, and garnet the 0.682, 0.954, and 0.997 probability intervals are $[0, 0.342]$, $[0, 0.648]$, and $[0, 0.862]$ and the corresponding intervals for prior distribution on Ca-pyroxene are $[0, 0.260]$, $[0, 0.447]$, and $[0, 0.496]$.

5. Results

We first consider an inversion where the parameters of the models are only constrained by the average moment of inertia. Next, we include the Love number k_2 as a further constraint. We also consider results for more restrictive settings on the parameters. In particular, a prior range of $[0.2, 0.3]$ for the Fe# , a chondritic bulk Fe/Si ratio of about $1.71 \pm 10\%$, and a core sulfur concentration of about 14wt%, all three of them are often used assumptions on the interior structure of Mars. Finally we discuss how the results change when a given mantle mineralogy can be assumed.

28

model parameter	parameter range
r_{cmb} [km]	$[1000, 2200]$
d_{crust} km	$[30, 90]$
ρ_{crust} [kg/m^3]	$[2700, 3100]$
X_{ol} [vol]	$[0, 1]$
X_{opx} [vol]	$[0, 1]$
X_{cpx} [vol]	$[0, 0.5]$
X_{gt} [vol]	$[0, 1]$
Fe# [at]	$[0.05, 0.40]$

Table 6: Model parameters and parameters range of core radius (r_{cmb}), crust thickness (d_{crust}) and density (ρ_{crust}), volume fractions of olivine, orthopyroxene, Ca-pyroxene, and garnet ($X_{\mathrm{ol}}, X_{\mathrm{opx}}, X_{\mathrm{cpx}}, X_{\mathrm{gt}}$) and iron number (Fe#).

5.1. MOI

Fig.[6] shows the core size as a function of core sulfur concentration for the hot and cold mantle temperature profiles for interior models that are constrained by the MOI. The smallest cores have a radius of about 1220km and are made of pure solid $\gamma - \mathrm{Fe}$, the largest cores with a 2200km core radius have core sulfur concentration of about 25wt%. Note that even larger cores are consistent with the MOI constraint if the sulfur concentration is above 25wt%. However, since the thermoelastic properties of our core model are derived from low sulfur concentration $\mathrm{Fe - S}$ liquids (see Appendix A) we don't expect them to be trustworthy for modeling cores with sulfur concentrations larger than 25wt%. The range of possible core sizes and the extension of the 3σ intervals for a given sulfur concentration are about identical for both the hot and the cold mantle models. If the core sulfur concentration were known, the core size would be known with a 3σ uncertainty of about 100km. Conversely, if the core radius were known precisely, then the 3σ uncertainty on the core sulfur concentration is about 3wt%.

The only mantle mineralogy parameters that are noteworthy constrained

29

Figure 6: Core size as a function of sulfur weight fraction for the hot and cold mantle temperature. Contours delimit domains corresponding to $0.997, 0.954, 0.682$ probability of occurrence. Cold (hot) mantle models that have more than 7.5wt% (3.5wt%) of sulfur have fully molten cores. The insets correspond to the individual 0.997 probability domains of the models with an inner core and without an inner core for cold and hot mantle models.

30

by the *MOI* datum is the volume fraction of garnet and the Fe# of the cold mantle models. Compared to the prior's 3σ interval the range of volume fraction of garnet is reduced from about $[0, 86]$vol% to about $[0, 77]$vol%. Since garnet does not experience a phase transition and remains stable to at least 23GPa before it transforms to denser phases like perovskite, a pure cold garnet mantle has a mass distribution that results in models that fail the *MOI* constraint. In order to agree with the mass constraint, the hot models have on average a somewhat larger Fe# (about 5at%) and for cold models the maximal Fe# at 3σ is about 4at% smaller than the prior value.

Interior models with cold mantles can have an inner core for core sulfur concentrations up to 7.5wt%, whereas the cores of hot mantle models that have a 275K higher temperature at the core mantle boundary, are completely molten if the sulfur concentration is larger than about 3.5wt% (Fig.[7]). The models with the largest possible inner cores are almost made of pure solid iron and in order to satisfy the global mass constraint have the smallest core radius. Cold mantle models that have an inner core can have core sizes up to about 1570km, while the core radius for hot mantle models is about 110km smaller. Models that have a pure iron solid core have core radii in a $[1249, 1401]$km range. Note that in contrast to the core sulfur concentration that decreases from its maximal value for models with almost no inner core, to zero sulfur for models with entirely solid cores, the sulfur concentration of the liquid core is almost constant for models with an inner core. For cold mantle models it is in a $[6.9, 7.4]$wt% interval and for hot models in a $[2.8, 3.3]$wt% interval. This is related the $Fe - S$ melting law (see (2)) which shows only a small variation in melting sulfur weight fraction when the core mantle boundary temperature is constant and the pressure variation at the core mantle boundary is small. Models with an inner core have a core mantle boundary pressure in the $[22, 26]$GPa range.

Neither the mantle mineralogy, nor the crust are appreciably constrained from the *MOI* data alone. Furthermore, even if the precision on the *MOI* was higher, as long as the mineralogy of the mantle and to a lesser extent the temperature of the mantle are not known more precisely, the uncertainty on the

31

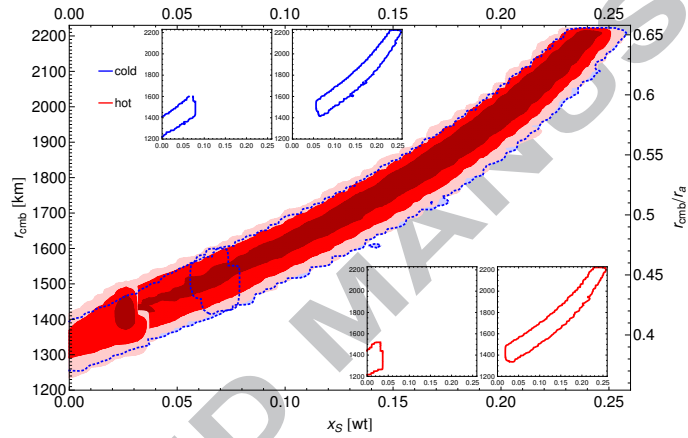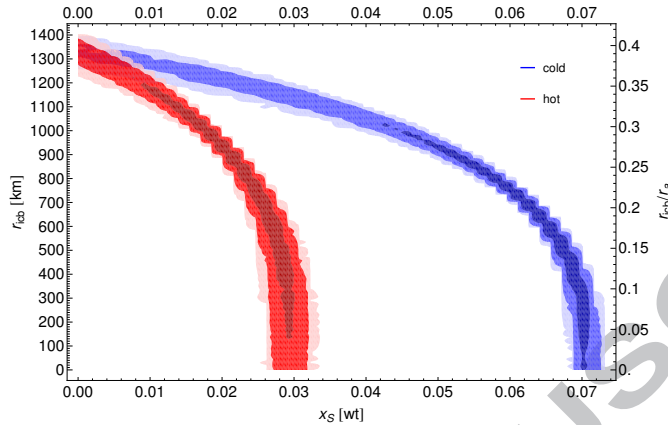Figure 7: Inner core size as function of sulfur weight fraction for the hot and cold mantle temperature. Contours delimit domains corresponding to $0.997, 0.954, 0.682$ probability of occurrence.

estimated core size remains substantial.

5.2. MOI and k_2

The range of possible core sizes can be drastically reduced if the tidal Love number k_2 is introduced as a further constraint since tides are sensitive to the depth of a liquid layer (see Fig.[8] and Fig.[9]). Both the core size and the core sulfur concentration increase with increasing k_2, since models with larger cores are more easily deformable and therefore result in larger external potential variations and models with larger cores have larger fractions of sulfur in order to be consistent with the global planet mass constraint.

For the most recent determination of k_2 (Konopliv et al., 2011, see Table [1]), the results show that the Mars models within the 3σ domains cannot have a solid inner core and that the cores of those models are entirely liquid (Fig.[8]). On the other hand, with the k_2 value of Marty et al. (2009) interior models with an inner core cannot be excludes at the 3σ level (see Fig.[8]). The absence of an inner core as a result of the large fraction of sulfur in the core is in agreement with the absence of a global magnetic field and suggests that an early geodynamo

32
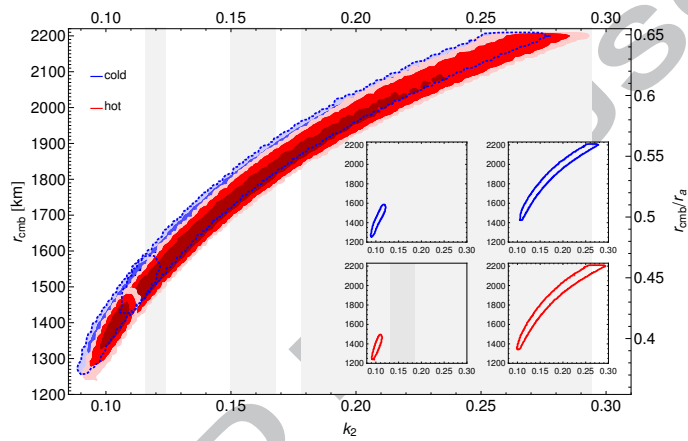
Figure 8: Core size as function of k_2 for the hot and cold mantle temperature for models that satisfy the MOI. Contours delimit domains corresponding to $0.997, 0.954, 0.682$ probability of occurrence. The gray shaded areas represent the k_2 values of Marty et al. (2009), Konopliv et al. (2011), and Smith et al. (2009) (from left to right). The insets correspond to the individual 0.997 contours of the models with an inner core and without an inner core for cold and hot mantle models.

33
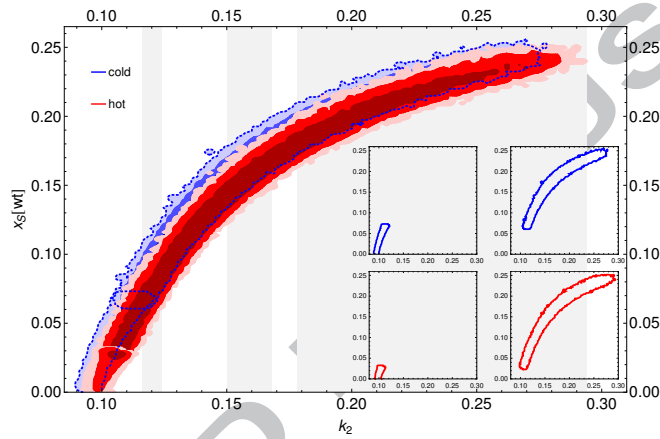
Figure 9: Core sulfur fraction as function of k_2 for the hot and cold mantle temperature for models that satisfy the MOI. Contours delimit domains corresponding to $0.997, 0.954, 0.682$ probability of occurrence. The gray shaded areas represent to the k_2 values of Marty et al. (2009), Konopliv et al. (2011), and Smith et al. (2009) (from left to right). The insets correspond to the individual 0.997 contours of the models with an inner core and without an inner core for cold and hot mantle models.

34

can only be of thermal origin (e.g. Stevenson, 2001).

If the mantle temperature profile is between our two temperature end-members, then at 1σ the estimated core radii are between 1729km and 1859km and the core sulfur concentration is in a [13.9, 17.8]wt% range (see Table [7] and Fig.[9]). Our estimated 1σ interval comprises the large core sulfur concentrations proposed in the bulk Mars models of Dreibus and Wänke (1985) (14wt%), Sanloup et al. (1999) (17wt%), and Mohapatra and Murty (2003) (17wt%), but not the smaller value of 10.5wt% of Lodders and Fegley (1997).

Our 1σ core radii interval does not comprise the estimated core size of 1680km found by Khan and Connolly (2008). This result is expected since Khan and Connolly (2008) have used the k_2 value of Yoder et al. (2003) which is smaller than the one of Konopliv et al. (2011) we use here (see Table [5]) and since k_2 increases with increasing core size. Their estimate is included in our 2σ interval for the core size. However, their deduced core sulfur concentration of $22 - 25$wt% (calculated from the inferred average core density) is not comprised and does not overlap with our estimated 3σ interval. Our results on the core size are also comparable to the core radii range of [1650, 1830]km obtained by Zharkov et al. (2009). Since those authors use the comparatively smaller k_2 value of Konopliv et al. (2006) (see Table [5]) there results also favor interior models with smaller cores. By construction, the interior models of Zharkov et al. (2009) have a core sulfur concentration of 14wt%. In order to be consistent with the geodesy constraints, mass, MOI, and k_2, the interior models of Zharkov et al. (2009) use a variable Fe# and up to 50mol% of hydrogen in the core.

Cold mantle models can have somewhat larger core radii (Fig.[10a]) than hot mantle models because the density of their silicate shell is smaller and since k_2 increases with increasing core size and silicate shell density. Although hot and cold mantle models have about the same mantle density because the temperature effect on mantle density is compensated by the lower Fe# for the colder models (Fig.[10d]), colder models with a core richer in sulfur with respect to the hotter models nevertheless have less dense silicate shell (Fig.[10g]) since

35

in order to satisfy the *MOI* constraint (with their to some extent larger cares) have somewhat lower crust densities (Fig.[10c]).

The data do not constrain the parameters of the crust as can be seen in Fig.[10b] and Fig.[10c]. On the other hand, the bulk Fe/Si ratio is estimated to be in a [1.34, 1.76] interval at 1σ and includes the chondritic Fe/Si value of 1.71 (Table [7] and Fig.[10f]). The most probable estimate for the Fe/Si ratio of Khan and Connolly (2008) is 1.2. This is significantly lower than the chondritic Fe/Si but still comprised in our estimated 3σ interval (see Table [7]). Since the estimated values of core radii and Fe# of Khan and Connolly (2008) are comparable to our results, their low Fe/Si estimate is a consequence of their overestimated core sulfur concentration. Our results on the Fe/Si ratio are consistent to those obtained by Zharkov et al. (2009) ([1.55, 1.78]). Note that all their interior models that are within that Fe/Si ratio range contain a significant fraction of hydrogen in the core.

The constraints on the mantle mineralogy parameters obtained by using the *MOI* and the k_2 value are very similar to those obtained from the *MOI* alone, i.e., a reduction of the width of the estimated 3σ probability interval of garnet compared to the width of the prior's 3σ and somewhat reducing the likelihood for cold mantle models with high values of the Fe# number (Fig.[10l], Fig.[10d], and Table [7]). The estimated 3σ intervals of olivine, orthopyroxene, and Ca-pyroxene (Table [7]) are very close to those of their prior distributions. However, the shape of the inferred distributions is notably different, compared to their prior distributions and intermediary values of about 20vol% are favored (see Figs.[10i,10j,10k,10l]).

An important but yet undecided issue on the mantle of Mars is the presence or not of a perovskite layer at the bottom of the mantle, which has profound consequences for Mars' thermal evolution and the present thermal state (e.g. van Thienen et al., 2006). It has also been invoked as a possible mechanism responsible for the formation of Mars' major volcanic centers (e.g. Zuber, 2001). The pressure at the core mantle boundary of the models that comply with the *MOI* and k_2 data can be as high as about 21.6GPa (Table [7]). This pressure

36

is too low for the phase transition to perovskite to occur if the phase transition data of Ito and Takahashi (1989) is adopted as we have in our modeling of the mantle. However, the precise pressure and temperature conditions for the phase transition are not known (e.g. van Thienen et al., 2006) and could occur at pressures as low as about 20GPa at 2250K and at about 21.2GPa at 1880K according to the data of Irifune et al. (1998). Therefore, for hot mantle models there is a small likelihood for a thin perovskite layer (about 200km) at the bottom of the mantle, whereas for the cold mantle models it is very unlikely (Fig.[10h]).

5.3. MOI, k_2, and compositional assumptions

We now discuss how compositional assumptions can further constrain the inferences about the model parameters. First, we use the core sulfur concentration of 14.2 ± 1wt%, which is used in recent Mars interior models (e.g Sohl and Spohn, 1997; Bertka and Fei, 1998; Zharkov and Gudkova, 2005; Zharkov et al., 2009) based on the chemical model for the bulk of Mars of Dreibus and Wänke (1985). We also assume a tighter range for the Fe# prior distribution, [0.2, 0.3] instead of [0.05, 0.4], since the Fe# of recently published Mars mantle fall within that range (see Table [2]). Next, we assume that the bulk Mars model has a Fe/Si ratio of 1.71 as in the mineralogy model of Dreibus and Wänke (1985). Finally we discuss how parameter inferences are modified if both a chondritic Fe/Si ratio and a core sulfur concentration of are assumed 14.2 ± 1wt%, the working hypothesis of the above cited Mars interior models.

Imposing the Fe# to be in a [0.2, 0.3] interval changes significantly only the volume fraction of garnet. The upper bound of the 3σ interval for hot mantle models is reduced from 65vol% to 34vol% and for cold mantle models from 75vol% to 51vol%. It also slightly shifts the estimates of the core radius towards lower values: those of the cold mantle by about 20km and those of the hot mantle models by about 10km.

Knowledge of the core sulfur concentrations in a tight interval leads to a more precise determination of the core radius as expected from the relation between x_S

37

and r_{cmb} (Fig.[6]). Moreover, since $x_{\text{S}} = 14.2\text{wt}\%$ is smaller than the estimated median value for x_{S} (Table [7]), this assumed core sulfur concentration results in somewhat smaller core radii. If the core sulfur concentration is $14.2\text{wt}\%$ with a $1\text{wt}\%$ uncertainty, which is significantly smaller than the estimated 1σ interval obtained from the MOI and k_2 data, then the core median and 3σ uncertainty change for cold (hot) mantle models from $1810 \pm 153\text{km}$ ($1784 \pm 159\text{km}$) to $1772 \pm 100\text{km}$ ($1765 \pm 118\text{km}$). The uncertainties of the cold (hot) models decreases by about 39km (18km). Inferences about the other parameter show no appreciable changes when the core sulfur concentration is fixed.

A significantly stronger constraint on the parameters of the interior structure models is obtained if a value for the Fe/Si ratio is assumed. Since it is a bulk property it influences the parameters related to both the core and mantle. Here we assume the chondritic value of $1.71 \pm 1\%$ for the Fe/Si ratio. The most likely Fe/Si ratio of the models constrained by k_2 and MOI is about 1.5, therefore imposing Fe/Si $= 1.71 \pm 1\%$ gives a higher likelihood to models that have more iron in the mantle and the core. Models with more iron in the core are either larger or have less sulfur for a given size. However, the geodesy data imposes a specific relation between core size and core sulfur concentration, as discussed above, which limits the iron concentration in the core (Fig.[11a] and Fig.[11c]). Therefore a chondritic Fe/Si value favors mantles that have a larger Fe# (Fig.[11b]). Since olivine contains more iron than pyroxenes and garnet (see Table [B.13]) models with more olivine are more likely (Fig.[11d]). The Fe/Si constraint and the resulting higher Fe# results in a significantly shortened interval on the volume fraction of garnet (Fig.[11g]). The inferences on the other parameters are not significantly altered by the Fe/Si constraint and the precision on the estimated core radius is not improved.

If the Fe/Si $= 1.71 \pm 1\%$ and $x_{\text{S}} = 14.2 \pm 1\text{wt}\%$ assumptions are used together then the 1σ uncertainty range on the core size is reduced by about 15km. Since resulting from the x_{S} constraint the interior models have somewhat smaller cores, models with larger Fe# numbers and larger volume fractions of olivine are more likely. The effect is more significant for cold mantle models, where the

38

median core size is reduced by about 50km and the median volume fraction of olivine increased by 27vol%. The inferences on the other parameters are not significantly altered.

5.4. Results for assumed mantle mineralogies

We investigate whether and by how much the precision on the interior model parameters can be increased by assuming a mineralogy for the mantle. We discuss in detail parameter inferences for the mantle mineralogy model DW84 and also compare briefly with estimates obtained for the LF97, EH45, EH70, and MM03 models. Finally, we address the question of whether interior structure models of Mars that are based on the DW84 mantle mineralogy and are consistent with the geodesy data can have simultaneously a core sulfur concentration of 14.2wt% and a bulk chondritic Fe/Si ratio or if those models require lower Fe/Si ratios as claimed by Sohl and Spohn (1997), Bertka and Fei (1998), Zharkov and Gudkova (2005), and Zharkov et al. (2009).

The inferred probability density functions of the mineral modes and of the Fe# of the models constrained by the MOI and by k_2 (Figs.[10i,10j,10k,10l,10d]) show that the separate volume fractions and Fe# of the here considered mantle models (Table [2]) have almost all an appreciable probability of occurrence. In particular, with the exception of the orthopyroxene fraction of the EH70 model, the volume fractions of the mineral modes and Fe# of the chosen mantle models are all within the estimated 2σ probability intervals (Table [7]). Therefore, by assuming one of the above mantle mineralogies the estimated precisions on the model parameters do not significantly improve if compared to the parameter precisions obtained from MOI and k_2 constrained models (see Tables [9,10] and Table [7]). The exceptions are the density and thickness of the crust for all cold mantle models but the EH70 model: the geodesy data favors thick crusts with a low density (Tables [9,10] and Figs. [14b,14c]). If the crust thickness and density were known more precisely and the Mars mantle mineralogy close to one of the above considered, then our result show that hotter mantle temperature than our cold end-member are more likely.

39

The inferred joint probability density on core size and core sulfur concentration for the DW84 model is shown in Fig.[12]. The figure shows that even if the temperature of the mantle were known more precisely the precision on the core size would not be improved significantly. However, it would be improved if the core sulfur concentration were known.

The DW84 models with the hot temperature profile have larger Fe/Si ratios (at 3σ) than the chondritic value of 1.71 (Table [10]). However, for cold mantle models our results show that contrarily to the results of Sohl and Spohn (1997), Bertka and Fei (1998), Zharkov and Gudkova (2005), and Zharkov et al. (2009), it is possible to construct interior models of Mars with the DW84 mantle mineralogy that have a chondritic Fe/Si ratio and a core sulfur concentration of 14.2wt% (see Fig.[13]). Note that those authors used larger values for the MOI, other mantle temperature profiles, other thermoelastic data for the mantle phases, and modeled the properties of the liquid core with equations of state parameters of solid Fe and FeS.

The temperature, pressure, density, and seismic velocity profiles for the models with the DW84, LF97, EH45, EH70, and MM03 mantle mineralogies are shown in Figs. [15, 16, 17, 18]. For all the profiles the estimated median core radius from the geodesy data is used. The values of the other model parameters and computed geodesy quantities are given in Table [8].

6. Discussion and conclusion

We have built detailed models of the interior structure of Mars. Our models use recent data on melting conditions of Fe − S and thermoelastic properties of liquid Fe − S for the core. We have parameterized the mineralogical composition of the mantle by its iron concentration and by the volume fractions of the low pressures mineral phases olivine, orthopyroxene, Ca-pyroxene, and garnet. Since it is difficult to ascertain the temperature in the mantle, we here used two end-member mantle temperature profiles that are deduced from studies dedicated to the thermal evolution of Mars. For a given set of model parameter values,

40

our model determines the mantle mineralogy changing with depth, the state of the core (liquid, solid, or both) and allows to calculate the density and elastic moduli of the whole planet together with the temperature and the concentration of sulfur in the core. From the resulting density profile the moment of inertia of the planet has been be calculated and from the density and elastic moduli profiles the Love number k_2 has been computed.

The goal of this study is to investigate which parameters of the interior of Mars can be constrained by two geodesy data: the moment of inertia and the Love number k_2. Here we use the most recent estimation of the moment of inertia and Love number k_2 of Konopliv et al. (2011). Our results show that, independently of the mineralogy of the mantle and the density and thickness of the crust, the radius and the concentration of sulfur in the core can be well determined from the geodesy data. The estimated 1σ intervals for the radius and core sulfur concentration are $[1729, 1859]$km and $[14, 18]$wt%. For other or additional light elements in the core than sulfur, the concentration would be different since the density would be different, but the estimated range of plausible core sizes would stay almost unchanged. Similarly, the core size estimate would not change appreciably if sulfur were not affecting the compressibility of liquid Fe at pressures larger than 15GPa, as suggested by Morard et al. (2008). If the compressibility of liquid Fe is assumed for the $Fe - S$ liquid then the estimated concentration of light elements in the core will be shifted to lower values by less than about 2wt%. If sulfur is the only light element in the core, and if the temperature of the mantle of Mars is not significantly cooler than our cold end-member, then the estimated large core sulfur concentration precludes the presence of a solid inner core at the 3σ level.

We have also shown that a perovskite layer at the bottom of the mantle could be possible for the hot mantle temperature end-member but not for the cold mantle temperature end-member. The geodesy data do almost not constrain the density and thickness of the crust and the mineralogy of the mantle. The large uncertainty on the mantle mineralogy results in a large range of possible Fe/Si ratios which comprises the chondritic value of 1.71. In order to obtain

41

more specific insight on the mineralogy of the mantle, bulk compositional constraints like a fixed Fe/Si ratio and a given concentration of light elements in the core have to be assumed.

The core size estimate can be more precise if the core sulfur concentration and the crust density and thickness are precisely known. If the sulfur concentration were known precisely then the 3σ interval for the core size would be reduced by about 100km. For the case where both the sulfur concentration and the crusts were known the 3σ interval would decrease by a further 40km.

We have also investigated if our knowledge on the core and the crust can be improved if a mineralogy model for the mantle of Mars is assumed. For the five tested mantle mineralogy models, our results show that the uncertainties on the parameters of the core, radius, and sulfur concentration, are only slightly reduced. Somewhat more precise estimates on the core parameters can also be obtained if the mantle temperature is better constrained than by our two end-members. In this case the crust density and thickness can also be constrained, especially if the temperature of the mantle is colder than our hot temperature end-member.

More precisely known geodesy data will improve our knowledge about the core parameters only to a certain extent. A perfectly known MOI value would lead to a marginally more precise core size estimate and a perfectly known k_2 value would decrease the core radius 3σ uncertainty to 110km. Significant better but difficultly assessable knowledge on the mantle mineralogical and temperature together with a precise knowledge of the crust parameters would further improve the core parameters. However, a definite answer on the question of the precise radius of the core can only be obtained with the advent of the deployment of a seismic network on the surface of Mars.
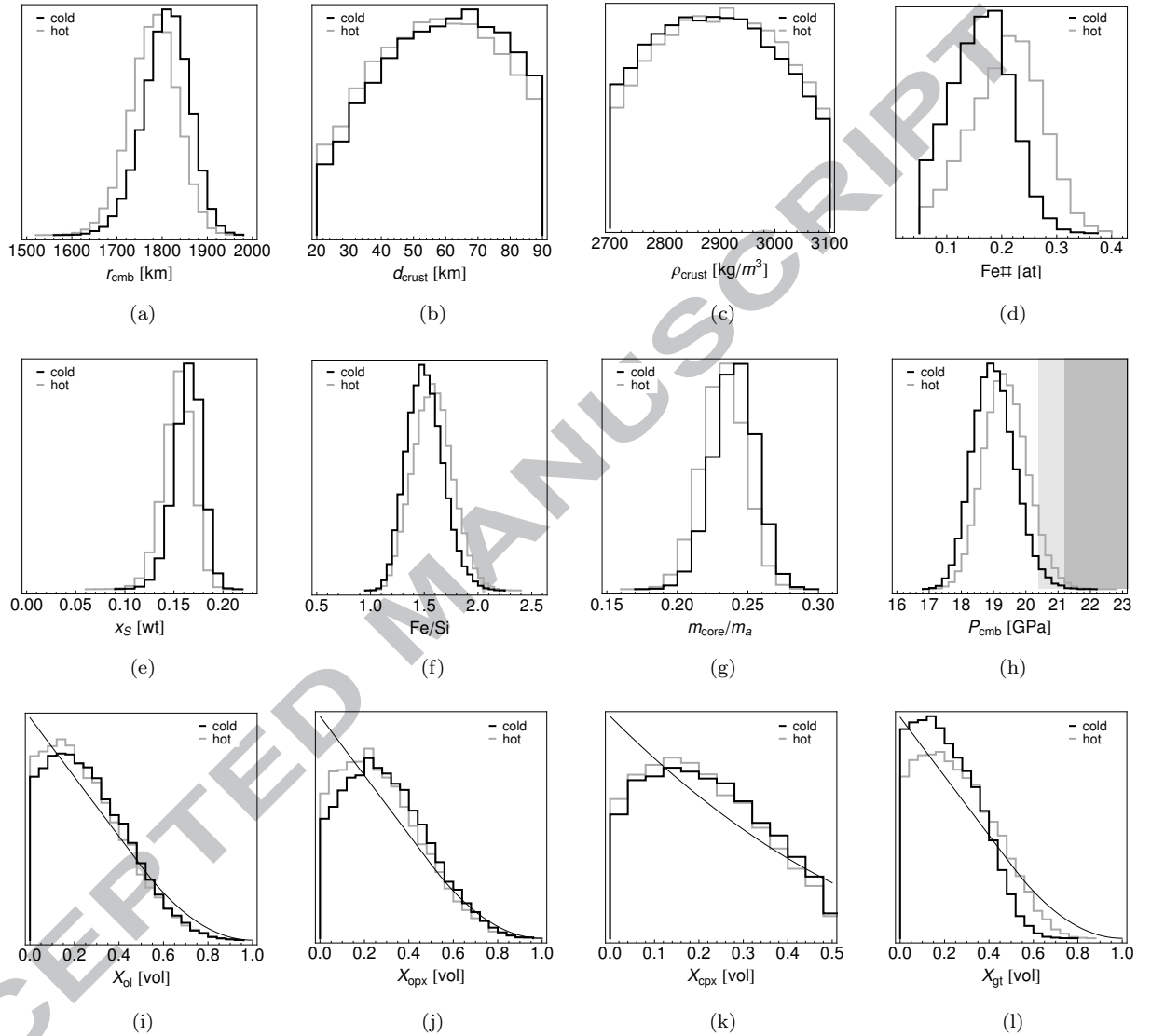
Figure 10: Probability density function for core size (a), crust thickness (b), crust density (c), mantle iron number (d), core sulfur fraction (e), bulk Fe/Si (f), core mass (g), pressure at the core mantle boundary (h) and mantle volume fraction of olivine (i), orthopyroxene (j), Ca-pyroxene (k), and garnet (l) for hot (gray) and cold (black) mantle temperatures that agree with k_2. The black curve in (i), (j), (k), and (l) is the probability density functions of the parameters prior distributions. The shaded areas in (h) corresponds to the pressure of the transition to perovskite, lighter gray: $T = 2250K$ and darker gray: $T = 1880K$ (Irifune et al., 1998).

	T	med.	68.2%	95.4%	99.7%
r_{cmb} [km]	c	1810.	[1758., 1859.]	[1701., 1900.]	[1640., 1945.]
	h	1784.	[1729., 1832.]	[1673., 1879.]	[1607., 1924.]
d_{crust} [km]	c	61.	[39., 79.]	[25., 88.]	[20., 90.]
	h	57.	[37., 77.]	[24., 88.]	[20., 90.]
ρ_{crust} [kg/m^3]	c	2885.	[2769., 3011.]	[2713., 3083.]	[2701., 3099.]
	h	2904.	[2781., 3022.]	[2716., 3085.]	[2701., 3099.]
x_{S} [wt]	c	0.17	[0.15, 0.18]	[0.13, 0.19]	[0.113, 0.199]
	h	0.16	[0.14, 0.17]	[0.12, 0.18]	[0.099, 0.191]
Fe/Si	c	1.50	[1.34, 1.68]	[1.21, 1.88]	[1.104, 2.062]
	h	1.58	[1.40, 1.77]	[1.24, 1.96]	[1.128, 2.148]
m_{core}/m_a	c	0.2404	[0.2252, 0.2550]	[0.2095, 0.2683]	[0.1941, 0.2822]
	h	0.2327	[0.2171, 0.2474]	[0.2020, 0.2617]	[0.1861, 0.2759]
$I_{\mathrm{core}}/m_a r_a^2$	c	0.0743	[0.0657, 0.0830]	[0.0573, 0.0912]	[0.0495, 0.1005]
	h	0.0697	[0.0613, 0.0782]	[0.0534, 0.0868]	[0.0455, 0.0959]
MOI	c	0.3645	[0.3640, 0.3650]	[0.3635, 0.3655]	[0.3630, 0.3660]
	h	0.3645	[0.3640, 0.3650]	[0.3635, 0.3655]	[0.3630, 0.3660]
k_2	c	0.158	[0.149, 0.167]	[0.140, 0.175]	[0.131, 0.185]
	h	0.158	[0.149, 0.167]	[0.141, 0.176]	[0.131, 0.185]
X_{ol} [vol]	c	0.241	[0.078, 0.454]	[0.013, 0.667]	[0.001, 0.832]
	h	0.229	[0.074, 0.447]	[0.012, 0.667]	[0.001, 0.819]
X_{opx} [vol]	c	0.279	[0.103, 0.496]	[0.017, 0.702]	[0.001, 0.862]
	h	0.250	[0.084, 0.470]	[0.015, 0.687]	[0.001, 0.844]
X_{cpx} [vol]	c	0.210	[0.073, 0.373]	[0.012, 0.474]	[0.001, 0.498]
	h	0.193	[0.067, 0.349]	[0.010, 0.466]	[0.001, 0.497]
X_{gt} [vol]	c	0.195	[0.064, 0.367]	[0.010, 0.509]	[0.001, 0.631]
	h	0.238	[0.079, 0.444]	[0.012, 0.607]	[0.001, 0.744]
Fe# [at]	c	0.165	[0.106, 0.218]	[0.063, 0.268]	[0.051, 0.318]
	h	0.212	[0.141, 0.271]	[0.080, 0.324]	[0.052, 0.376]
P_{cmb} [GPa]	c	19.0	[18.4, 19.7]	[17.8, 20.4]	[17.3, 21.2]
	h	19.4	[18.7, 20.0]	[18.1, 20.8]	[17.5, 21.6]

Table 7: Estimated median and probability intervals for core size, crust thickness, crust density, core sulfur concentration, Fe/Si , core mass, core moment of inertia, k_2, volume fraction of olivine, orthopyroxene, Ca-pyroxene, and garnet, Fe# , and pressure at the core mantle boundary for models that satisfy the geodesy constraints on MOI and k_2.

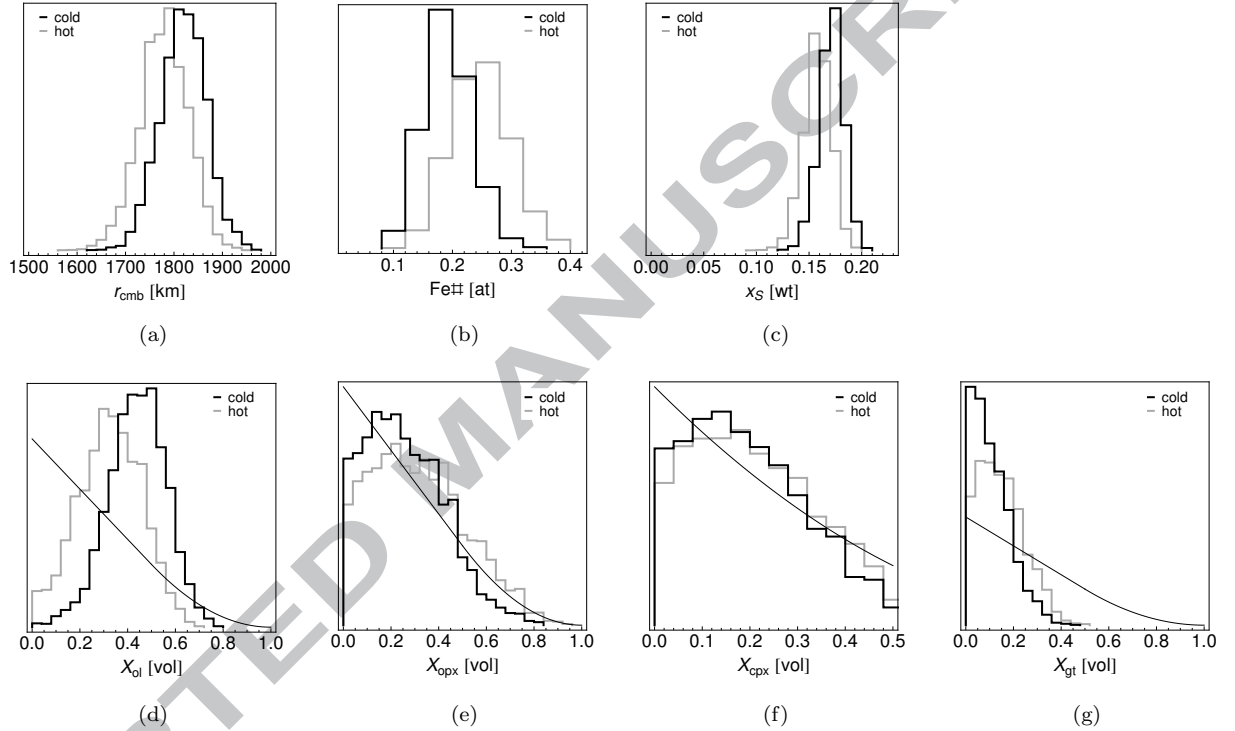Figure 11: Probability density function for core size (a), mantle iron number (b), core sulfur fraction (c) and mantle volume fraction of olivine (d), orthopyroxene (e), Ca-pyroxene (f), and garnet (g) for hot (gray) and cold (black) mantle temperatures that agree with k_2 and where $Fe/Si = 1.71 \pm 1\%$. The black curve in (d), (e), (f), and (g) is the probability density functions of the parameters prior distributions.

45

	$r_{\rm cmb}$	$d_{\rm crust}$	$\rho_{\rm crust}$	$x_{\rm S}$	Fe/Si	$m_{\rm core}/m_a$	$I_{\rm core}/I_a$	MOI	k_2	$P_{\rm cmb}$	$T_{\rm cmb}$
	km	km	kg/m^3	wt						GPa	K
DW84	1731.	85.	2701.	0.17	1.83	0.2093	0.0592	0.3653	0.146	20.2	1880
	1756.	84.	2987.	0.16	1.93	0.2201	0.0640	0.3651	0.156	19.8	2150
LF97	1769.	86.	2776.	0.17	1.75	0.2214	0.0654	0.3652	0.151	19.7	1880
	1769.	60.	2785.	0.15	1.79	0.2274	0.0670	0.3640	0.157	19.6	2150
EH45	1727.	87.	2746.	0.17	1.65	0.2079	0.0585	0.3656	0.145	20.2	1880
	1763.	85.	2957.	0.16	1.75	0.2228	0.0653	0.3648	0.156	19.7	2150
EH70	1808.	60.	3066.	0.17	1.46	0.2379	0.0733	0.3652	0.158	19.0	1880
	1862.	26.	3062.	0.16	1.56	0.2595	0.0847	0.3637	0.174	18.3	2150
MM03	1783.	81.	2745.	0.17	1.71	0.2272	0.0681	0.3645	0.154	19.5	1880
	1776.	72.	3069.	0.16	1.75	0.2291	0.0681	0.3646	0.158	19.5	2150

Table 8: Model parameters and calculated geodesy quantities associated to the estimated median core radii from the MOI and k_2 data for the hot and cold DW84, LF96, EH45, EH70, and MM03 mantle models.
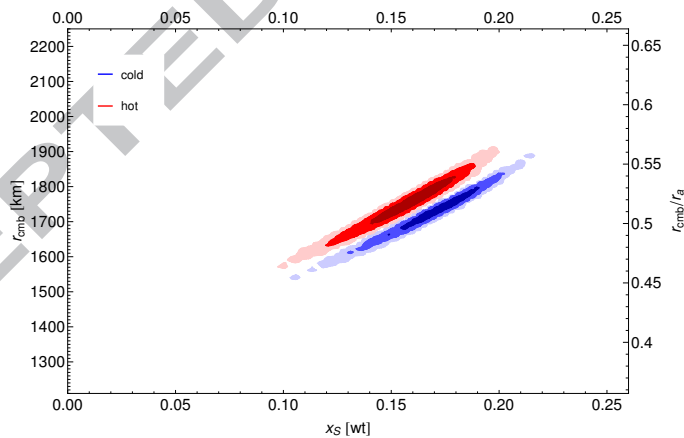
Figure 12: Core size as function of sulfur weight fraction for the hot and cold mantle temperature and the DW84 mantle mineralogy for models that agree with the MOI and the k_2. Contours delimit domains corresponding to $0.997, 0.954, 0.682$ probability of occurrence.

46
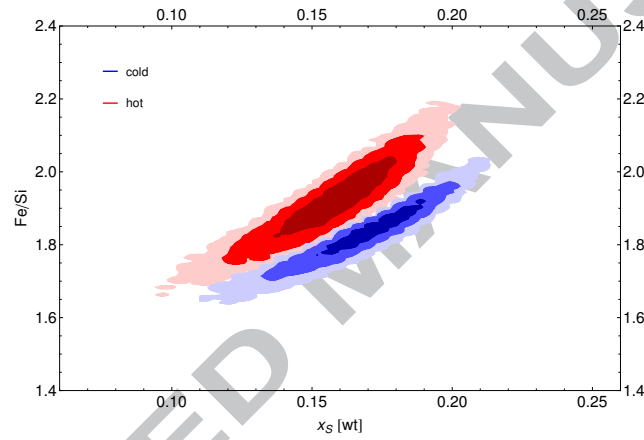
Figure 13: Fe/Si ratio as function of sulfur weight fraction for the hot and cold mantle temperature and the DW84 mantle mineralogy for models that agree with the MOI and the k_2. Contours delimit domains corresponding to $0.997, 0.954, 0.682$ probability of occurrence.
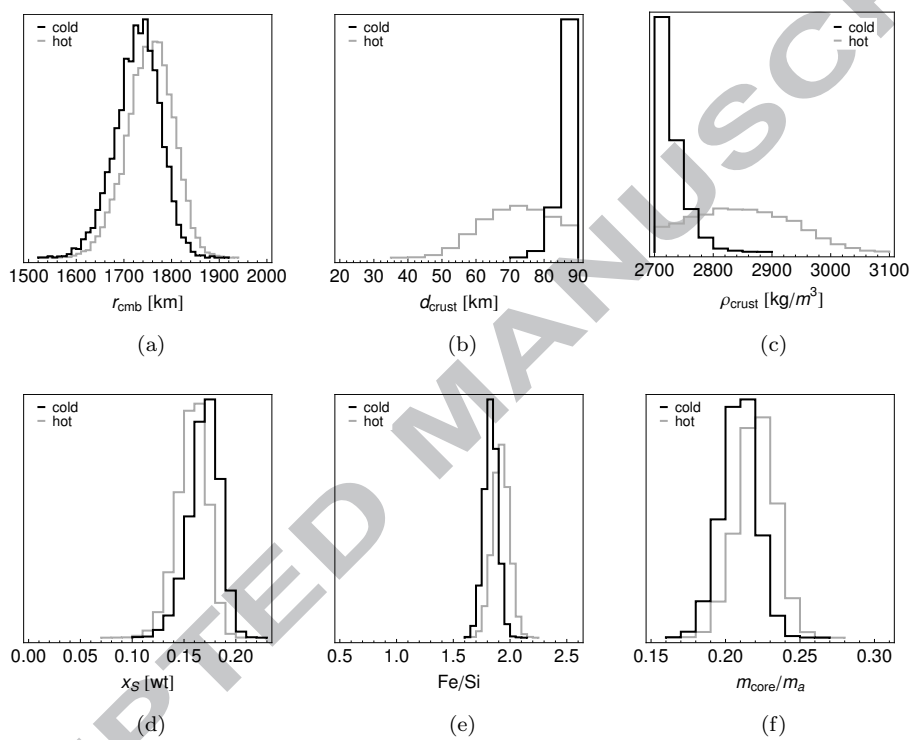
Figure 14: Probability density function for core size (a), crust thickness (b), crust density (c), core sulfur fraction (d), bulk Fe/Si (e), and core mass (f) for the DW84 mantle mineralogy and hot (gray) and cold (black) mantle temperatures.

48
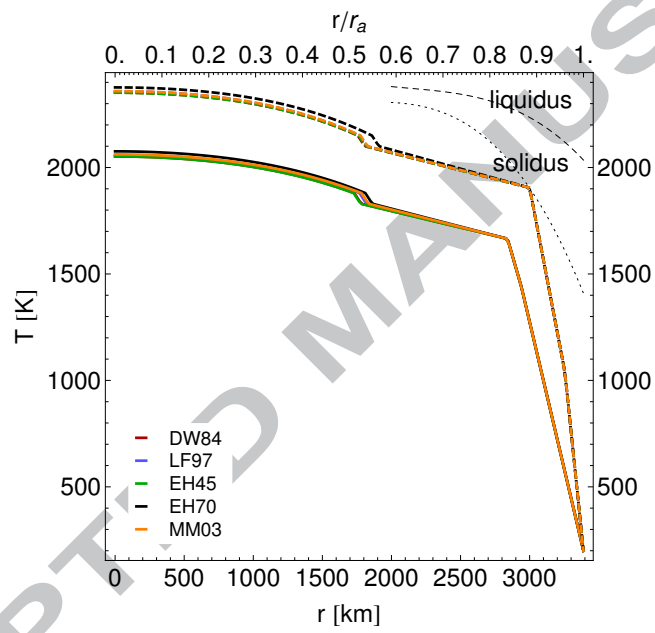
Figure 15: Temperature profiles as a function of radius for DW84, LF97, EH45, EH70, and MM03 mantle models. Solidus and liquidus curves are for Earth mantle anhydrous peridotite Takahashi (1990).

49
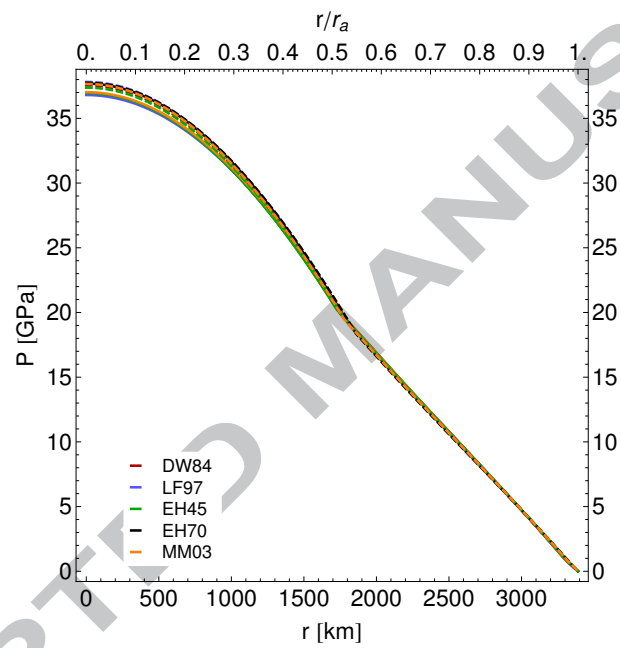
Figure 16: Pressure profiles as a function of radius for DW84, LF97, EH45, EH70, and MM03 mantle models for hot (dashed) and cold mantle temperature (continuous) end-member.
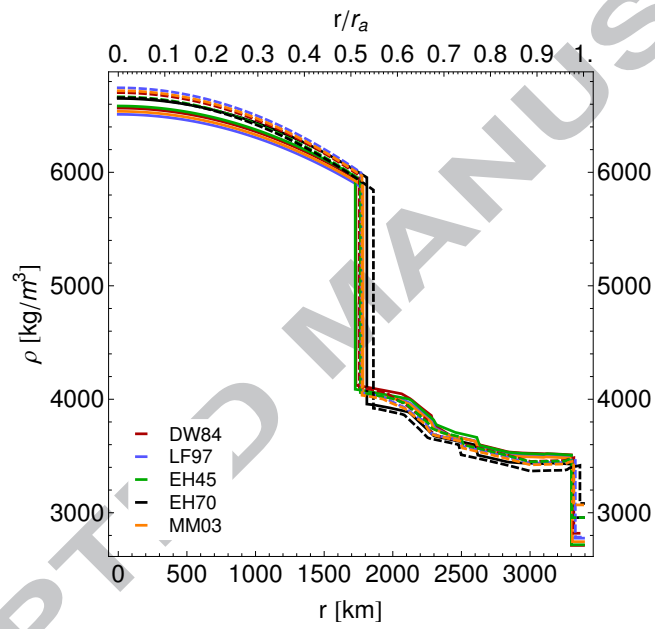
Figure 17: Density profiles as a function of radius for DW84, LF97, EH45, EH70, and MM03 mantle models for hot (dashed) and cold mantle temperature (continuous) end-member.
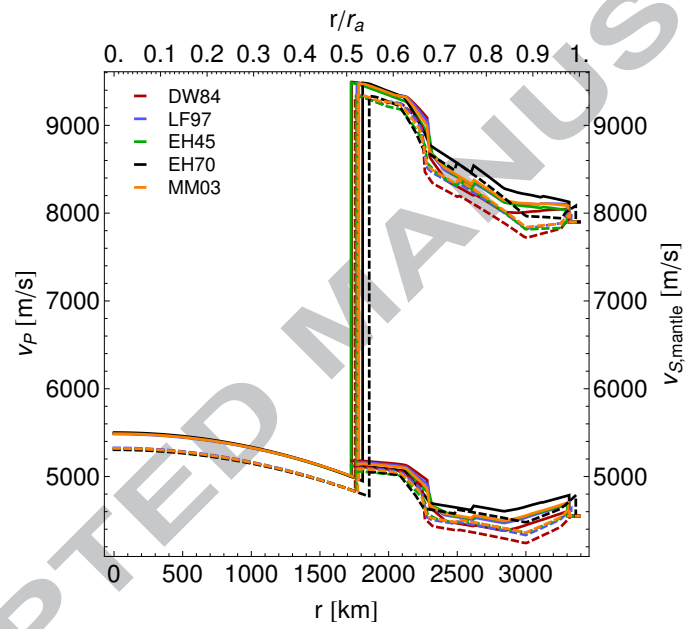
Figure 18: v_P profiles and mantle v_S profiles (bottom left) as a function of radius for DW84, LF97, EH45, EH70, and MM03 mantle models for hot (dashed) and cold mantle temperature (continuous) end-member.

		med.	68.2%	95.4%	99.7%
r_{cmb} [km]	DW84	1731.	[1682., 1774.]	[1628., 1815.]	[1574., 1859.]
	LF97	1769.	[1719., 1814.]	[1667., 1851.]	[1602., 1886.]
	EH45	1727.	[1680., 1773.]	[1628., 1811.]	[1560., 1848.]
	EH70	1808.	[1758., 1853.]	[1707., 1895.]	[1653., 1934.]
	MM03	1783.	[1733., 1828.]	[1678., 1870.]	[1612., 1912.]
d_{crust} [km]	DW84	88.	[85., 89.]	[80., 90.]	[76., 90.]
	LF97	86.	[80., 89.]	[74., 90.]	[68., 90.]
	EH45	88.	[84., 89.]	[80., 90.]	[74., 90.]
	EH70	54.	[41., 70.]	[31., 84.]	[23., 89.]
	MM03	82.	[75., 88.]	[68., 90.]	[60., 90.]
ρ_{crust} [kg/m^3]	DW84	2720.	[2705., 2748.]	[2701., 2787.]	[2700., 2838.]
	LF97	2740.	[2712., 2784.]	[2702., 2838.]	[2700., 2897.]
	EH45	2721.	[2706., 2750.]	[2701., 2789.]	[2700., 2831.]
	EH70	2921.	[2798., 3026.]	[2724., 3083.]	[2701., 3099.]
	MM03	2766.	[2722., 2825.]	[2704., 2887.]	[2700., 2954.]
x_{S} [wt]	DW84	0.17	[0.16, 0.18]	[0.14, 0.20]	[0.12, 0.21]
	LF97	0.17	[0.16, 0.19]	[0.14, 0.20]	[0.12, 0.21]
	EH45	0.17	[0.15, 0.18]	[0.14, 0.19]	[0.11, 0.20]
	EH70	0.17	[0.15, 0.18]	[0.13, 0.19]	[0.11, 0.20]
	MM03	0.17	[0.16, 0.19]	[0.14, 0.20]	[0.12, 0.21]
Fe/Si	DW84	1.84	[1.77, 1.89]	[1.71, 1.95]	[1.66, 2.01]
	LF97	1.75	[1.69, 1.81]	[1.64, 1.87]	[1.56, 1.94]
	EH45	1.65	[1.60, 1.70]	[1.54, 1.75]	[1.48, 1.80]
	EH70	1.47	[1.40, 1.53]	[1.34, 1.59]	[1.28, 1.66]
	MM03	1.71	[1.65, 1.78]	[1.58, 1.84]	[1.51, 1.90]
P_{cmb} [GPa]	DW84	20.2	[19.7, 20.8]	[19.2, 21.4]	[18.6, 22.1]
	LF97	19.7	[19.2, 20.3]	[18.7, 20.9]	[18.2, 21.7]
	EH45	20.2	[19.7, 20.8]	[19.2, 21.4]	[18.7, 22.1]
	EH70	19.1	[18.5, 19.7]	[18.0, 20.3]	[17.5, 20.9]
	MM03	19.5	[19.0, 20.1]	[18.5, 20.8]	[17.9, 21.6]

Table 9: Estimated median and probability intervals for core size, crust thickness, crust density, core sulfur concentration, Fe/Si , and P_{cmb} for the cold mantle models.   53

		med.	68.2%	95.4%	99.7%
r_{cmb} [km]	DW84	1756.	[1707., 1802.]	[1653., 1842.]	[1598., 1885.]
	LF97	1769.	[1720., 1816.]	[1668., 1856.]	[1602., 1890.]
	EH45	1763.	[1713., 1810.]	[1660., 1852.]	[1597., 1889.]
	EH70	1862.	[1828., 1893.]	[1797., 1925.]	[1762., 1954.]
	MM03	1776.	[1729., 1820.]	[1676., 1860.]	[1618., 1901.]
d_{crust} [km]	DW84	72.	[62., 83.]	[53., 89.]	[45., 90.]
	LF97	64.	[52., 78.]	[42., 87.]	[34., 90.]
	EH45	72.	[61., 83.]	[52., 89.]	[43., 90.]
	EH70	24.	[21., 30.]	[20., 39.]	[20., 52.]
	MM03	55.	[43., 70.]	[34., 84.]	[30., 89.]
ρ_{crust} [kg/m^3]	DW84	2846.	[2759., 2937.]	[2710., 3007.]	[2701., 3071.]
	LF97	2898.	[2786., 2998.]	[2717., 3068.]	[2701., 3097.]
	EH45	2845.	[2757., 2933.]	[2711., 3008.]	[2701., 3071.]
	EH70	3032.	[2941., 3081.]	[2822., 3097.]	[2718., 3100.]
	MM03	2933.	[2811., 3036.]	[2723., 3088.]	[2703., 3099.]
x_S [wt]	DW84	0.16	[0.14, 0.17]	[0.13, 0.18]	[0.11, 0.19]
	LF97	0.16	[0.14, 0.17]	[0.13, 0.18]	[0.10, 0.19]
	EH45	0.16	[0.15, 0.17]	[0.13, 0.19]	[0.10, 0.20]
	EH70	0.16	[0.15, 0.17]	[0.14, 0.18]	[0.13, 0.19]
	MM03	0.16	[0.14, 0.17]	[0.12, 0.18]	[0.10, 0.19]
Fe/Si	DW84	1.92	[1.85, 1.99]	[1.78, 2.06]	[1.71, 2.14]
	LF97	1.79	[1.72, 1.86]	[1.65, 1.93]	[1.58, 1.99]
	EH45	1.74	[1.68, 1.81]	[1.61, 1.87]	[1.54, 1.93]
	EH70	1.56	[1.52, 1.60]	[1.48, 1.65]	[1.45, 1.71]
	MM03	1.76	[1.66, 1.80]	[1.60, 1.87]	[1.53, 1.93]
P_{cmb} [GPa]	DW84	19.8	[19.3, 20.4]	[18.8, 21.1]	[18.2, 21.8]
	LF97	19.6	[19.0, 20.2]	[18.5, 20.8]	[18.1, 21.6]
	EH45	19.7	[19.2, 20.3]	[18.7, 21.0]	[18.2, 21.8]
	EH70	18.3	[18.0, 18.8]	[17.6, 19.2]	[17.2, 19.6]
	MM03	19.5	[19.0, 20.1]	[18.5, 20.7]	[18.0, 21.4]

Table 10: Estimated median and probability intervals for core size, crust thickness, crust density, core sulfur concentration, Fe/Si , and P_{cmb} for the hot mantle models.   54

Appendix A. Thermoelastic properties of the core

In order to calculate the densities of solid $\gamma - \mathrm{Fe}$ and the liquid $\mathrm{Fe} - \mathrm{S}$ solution at local core pressures and temperatures, we use equations of state (EoS) that express the density as a function of pressure and temperature. We correct separately the density for temperature and pressure.

At reference pressure, the local density at temperature T of the solid $\gamma - \mathrm{Fe}$ is given in terms of the thermal expansion coefficient α as

$$\rho_0(T) = \rho_{\mathrm{ref}} \exp\left[-\int_{T_{\mathrm{ref}}}^{T} dT' \alpha(T')\right]. \tag{A.1}$$

Here, T_{ref} is the reference temperature for $\gamma - \mathrm{Fe}$. EoS parameters at reference conditions for $\gamma - \mathrm{Fe}$ are given in Table (A.11). We use a subscript 0 to indicate that the density is calculated at the reference pressure P_{ref}: $\rho_0(T) = \rho(P_{\mathrm{ref}}, T)$.

We also calculate the elastic moduli at the local temperature T. These moduli are used for the calculation of the response of the models to tidal forcing and the isothermal bulk modulus K_T is needed for the calculation of the density at local pressure. The bulk modulus K_T and the shear modulus μ are assumed to depend linearly on temperature:

$$K_{T,0}(T) = K_{T,\mathrm{ref}} + \left(\frac{dK_T}{dT}\right)_T (T - T_{\mathrm{ref}}), \tag{A.2}$$

$$\mu_0(T) = \mu_{\mathrm{ref}} + \left(\frac{d\mu}{dT}\right)_T (T - T_{\mathrm{ref}}), \tag{A.3}$$

where the derivatives of K_T and μ with respect to temperature are assumed temperature independent. The values of the EoS parameters for solid $\gamma - \mathrm{Fe}$ at reference pressure are given in Table [A.11].

In order to calculate the thermoelastic properties of the liquid $\mathrm{Fe} - \mathrm{S}$ system we assume that the outer core liquid can be described by an ideal solution model (e.g. Callen, 1985). The use of this approximation is justified by the lack of thermoelastic data on iron rich iron-sulfur solutions at high pressures. Note nevertheless that lower pressure volume data ($10^5 \mathrm{Pa}$ and $4\mathrm{GPa}$) of iron rich $\mathrm{Fe} - \mathrm{S}$ solutions (Nagamori, 1969; Nishida et al., 2008) and liquidus curves (e.g. Chen et al., 2008, at $14\mathrm{GPa}$) exhibit significant deviations from non-ideality.

The molar volume of an ideal solution at temperature T and pressure P_0 is the molar fraction weighted sum of the molar volumes of each component. For a binary solution it is

$$V_0(\chi_S, T) = \chi_{Fe}V_{Fe}(T) + \chi_S V_S(T), \tag{A.4}$$

where V_{Fe} and V_S are the molar volumes of iron and sulfur in the solution at P_0, and χ_S and $\chi_{Fe} = (1 - \chi_S)$ are the molar fractions of sulfur and iron. The volume of each component i at pressure P_0 is calculated from its volume $V_{i,0}$ at reference temperature T_0 with (A.1).

The density of the solution at (P_0, T) is

$$\rho_0(\chi_S, T) = \frac{(1 - \chi_S)M_{Fe} + \chi_S M_S}{V_0(\chi_S, T)}, \tag{A.5}$$

where M_{Fe} and M_S are the molar masses of iron an sulfur and the weight fraction of sulfur x_S in the solution is

$$x_S = \left[1 + \left(\frac{1}{\chi_S} - 1\right)\frac{M_{Fe}}{M_S}\right]^{-1}. \tag{A.6}$$

From the definition of the isothermal bulk modulus, $K_T = -\frac{\partial P}{\partial \ln V}\big|_T$, the bulk modulus of the solution can be written as

$$K_{T,0}(\chi_S, T) = V_0(\chi_S, T)\left[\frac{(1 - \chi_S)V_{Fe}(T)}{K_{T,Fe}(T)} + \frac{\chi_S V_S(T)}{K_{T,S}(T)}\right]^{-1}, \tag{A.7}$$

where $K_{T,Fe}$ and $K_{T,S}$ are the bulk moduli of iron and sulfur in the solution. The bulk modulus of each component i at (P_0, T) is calculated from the reference value at (P_0, T_0) with (A.2).

The derivative of the K_T with respect to pressure of the Fe $-$ S liquid is calculated from Eq. (A.7). It is

$$K'_{T,0}(\chi_S, T) = -1 + \frac{K_{T,0}(\chi_S, T)^2}{V_0(\chi_S, T)} \\ \left[\frac{(1 - \chi_S)V_{Fe}(T)}{K_{T,Fe}(T)^2}(1 + K'_{T,Fe}) + \frac{\chi_S V_S(T)}{K_{T,S}(T)^2}(1 + K'_{T,S})\right], \tag{A.8}$$

where $K'_{T,i}$ is the derivative of the bulk modulus with respect to pressure of component i.

56

Finally, the thermal expansivity of the iron-sulfur solution can be derived from (A.4) by using the definition of the thermal expansivity $\alpha = \left.\frac{\partial \ln V(T)}{\partial T}\right|_P$. It is

$$\alpha(\chi_S, T) = \frac{(1 - \chi_S)V_{Fe}(T)\alpha_{Fe}(T) + \chi_S V_S(T)\alpha_S(T)}{V(\chi_S, T)}, \qquad (A.9)$$

where α_{Fe} and α_S are the thermal expansiveness of iron and sulfur.

To calculate the thermoelastic properties of the liquid solution and of solid $\gamma - Fe$ at local core pressures the temperature corrected EoS values are isothermally compressed. Here we use a finite strain Birch-Murnaghan equation of state derived from a fourth order expansion of the Helmholtz free energy in the Eulerian strain ε (Stixrude and Lithgow-Bertelloni, 2005) :

$$P = - (1 - 2\varepsilon)^{\frac{5}{2}} \left[3K_0\varepsilon - \frac{9}{2}K_0(K_0' - 4)\varepsilon^2 \right] \qquad (A.10)$$

$$K = (1 - 2\varepsilon)^{\frac{5}{2}} \left[K_0 - K_0\left(3K_0' - 5\right)\varepsilon + \frac{27}{2}K_0(K' - 4)\varepsilon^2 \right] \qquad (A.11)$$

$$K' = K_0' + \left[3K_0'^2 - 21K_0' + \frac{143}{3} \right]\varepsilon \qquad (A.12)$$

$$\mu = (1 - 2\varepsilon)^{\frac{5}{2}} \Big[\mu_0 + (5\mu_0 - 3\mu_0'K_0)\,\varepsilon \qquad (A.13)$$

$$+ \left(6K_0\mu_0' - 24K_0 - 14\mu_0 + \frac{9}{2}K_0K_0' \right)\varepsilon^2 \Big] \qquad (A.14)$$

with the Eulerian strain given as

$$\varepsilon = \frac{1}{2}\left[1 - \left(\frac{\rho}{\rho_0}\right)^{\frac{2}{3}} \right]. \qquad (A.15)$$

The superscript $\prime$ and $\prime\prime$ stand for first and second derivative with respect to pressure. The derivatives of the moduli are only weakly dependent on temperature and therefore evaluated at reference temperature. Since the core constituents are compressed at constant temperature K and K' stand for the isothermal bulk modulus and its derivative with respect to pressure.

In order to calculate deformations due to tidal forcing we need, beside the shear modulus μ, the adiabatic bulk modulus K_S. It is related to the isothermal

bulk modulus K_T through the fundamental thermodynamic relation (Poirier, 2000)

$$K_S(P,T) = K_T(P,T)[1 + \alpha(P,T)\gamma(P,T)T]. \tag{A.16}$$

As the temperature inside cores of terrestrial planetary exceeds the Debye temperature (Poirier, 2000), the product of the bulk modulus and thermal expansivity is approximatively pressure independent

$$\alpha(P,T)K_T(P,T) \approx \alpha(P_{ref},T)K_T(P_{ref},T). \tag{A.17}$$

Finally, we calculated the Grüneisen parameter γ from the Vashchenko and Zubarev formulation (Anderson, 2000)

$$\gamma(P,T) = \frac{\frac{1}{2}K'_T(P,T) - \frac{5}{6} + \frac{2}{9}PK_T^{-1}(P,T)}{1 - \frac{4}{3}PK_T^{-1}(P,T)}. \tag{A.18}$$

With the adiabatic bulk modulus, shear modulus, and density known at local (P,T) the seismic P- and S-wave velocities can be calculated from

$$v_P(P,T) = \sqrt{\frac{K_S(P,T)}{\rho(P,T)}}, \tag{A.19}$$

$$v_S(P,T) = 0, \tag{A.20}$$

for liquid phases, and

$$v_P(P,T) = \sqrt{\frac{K_S(P,T) + \frac{4}{3}\mu(P,T)}{\rho(P,T)}}, \tag{A.21}$$

$$v_S(P,T) = \sqrt{\frac{\mu(P,T)}{\rho(P,T)}} \tag{A.22}$$

for solid phases.

Although the data relevant to Mars' core pressure and temperature conditions is scarce, there is a sufficient amount of recent data on the liquid $Fe - S$ system for a first-order calculation. At reference conditions the density, the bulk modulus and its derivative with respect to pressure of sulfur in the $Fe - S$ solution is calculated from the EoS data of liquid iron (Anderson and Ahrens, 1994) and $Fe - 10wt\%S$ (Balog et al., 2003) with Eqs. (A.4, A.7, A.8). The thermal

58

	ρ	V	α	K_T	K_T'	dK_T/dT	μ	μ'	$d\mu/dT$
	kg/m^3	cm^3/mol	10^5/K	GPa		GPa/K	GPa		GPa/K
Solid: $P_{\text{ref}} = 10^5$Pa *and* $T_{\text{ref}} = 1573$K									
γ − Fe	7413.		7.7	103.	5.	−0.020	62.6	2.7	−0.03
Liquid: $P_{\text{ref}} = 10^5$Pa *and* $T_{\text{ref}} = 1881$K									
FeS		12.38	16.28						
Fe		7.96	9.20	85.	5.8	−0.031			
Fe − 10wt%S		9.45		63.	4.8				
S in Fe − S solution		17.19	19.2	39.	3.1				

Table A.11: Equation of state parameters for the core. Solid: γ−Fe from Ahrens et al. (2002). Liquid: Fe from Anderson and Ahrens (1994), FeS from Kaiura and Toguri (1979), and Fe − 10wt%S from Balog et al. (2003). Estimated EoS parameters for S in Fe − S solution.

expansivity at reference temperature of sulfur in the solution is computed from the temperature dependent density of liquid FeS (Kaiura and Toguri, 1979) and liquid Fe. As the temperature dependence of the bulk modulus of sulfur in the Fe − S is yet unknown, we calculate K_T of the solution at reference temperature and assume it to be linearly dependent on temperature (i.e. Eq. A.2), and use the $(dK_T/dT)_{\text{ref}}$ of liquid iron for the solution. The derivative of K_T with respect to pressure is evaluated at reference conditions and assumed temperature independent. The resulting EoS parameters for sulfur in the solution are given together with the EoS parameters of liquid Fe, FeS, and Fe − 10wt%S in Tab. (A.11).

Appendix B. Thermoelastic properties of the mantle

For a given temperature and pressure and mantle bulk composition, i.e., Fe# and volume fractions of the low pressure mineral phases olivine, orthopyroxene, clinopyroxene, and garnet, we determine the volume fractions of the high pressure mineral phases (Table [B.13]) at each depth inside the mantle by

using phase diagrams (Verhoeven et al., 2005). In order to obtain the density and elastic moduli at a given pressure and temperature, each mineral phase follows first an isobaric and then an isentropic thermodynamic path. The EoS parameters for the mineral phases of the mantle are given in Table [B.12]. Once the density and the elastic moduli of each mineral phase have been determined at local pressure and temperature, the phase aggregate's density is calculated from the volume fraction weighted sum of the densities of each phase and the elastic moduli by the Hashin-Shtrikman average (e.g. Poirier, 2000).

To calculate the thermoelastic properties of mineral phase i at a given pressure and temperature we proceed as follows: Since each mineral phase of our model is a solid solution among two species, i.e. a magnesium and an iron end-member, the thermoelastic properties of each phase are calculated from the thermoelastic properties of its species. The fraction of iron atoms within each phase determines the concentration of the iron end-member species. Here, we use a parametrization that is linear in the concentration of iron to specify the thermoelastic properties of a phase from the thermoelastic properties of the magnesium end-member. Following Vacher et al. (1998) and Verhoeven et al. (2005) we assume that for each phase i only the density $\rho_{0,i}$, the adiabatic incompressibility $K_{S0,i}$, and the shear modulus $\mu_{0,i}$ depend on the fraction of iron atoms y in the phase. We write:

$$\rho_{0,i}(P_0, T_0) = \rho_i(P_0, T_0) + y\,\rho_{0,\text{Fe},i}(P_0, T_0) \tag{B.1}$$

$$K_{S0,i}(P_0, T_0) = K_{S,i}(P_0, T_0) + y\,K_{S0,\text{Fe},i}(P_0, T_0) \tag{B.2}$$

$$\mu_{0,i}(P_0, T_0) = \mu_i(P_0, T_0) + y\,\mu_{0,\text{Fe}}(P_0, T_0), \tag{B.3}$$

where the subscripts "$_0$" means that those quantities are calculated at reference conditions, i.e., at P_0 and T_0, usually ambient condition, and the quantities to the right-hand side of the equality sign refer to the magnesium end-member species and to an iron fraction proportional correction. The fraction of iron atoms in each phase is determined from the bulk mantle composition and from phase diagrams.

Second, each individual phase i is heated at constant pressure, P_0, from the

60

reference temperature T_0 to an intermediary temperature ϑ_i, called the foot of the adiabat (to be defined later), by using Eq. (A.1). Following Trampert et al. (2001) we calculate the adiabatic bulk modulus at ϑ_i from

$$K_{S,i}(P_0, \vartheta_i) = K_{S0,i}(P_0, T_0) \left(\frac{\rho_i(P_0, \vartheta_i)}{\rho_{0,i}(P_0, T_0)} \right)^{\delta_{S0,i}}, \qquad (B.4)$$

where δ_{S0} is the Anderson-Grüneisen parameter, defined as follows (e.g. Stacey and Davis, 2008)

$$\delta_{S0,i} = -\frac{1}{\alpha_i(P_0, T_0)} \left(\frac{\partial \ln K_{S,i}}{\partial T} \right)_{P_0}. \qquad (B.5)$$

The value of the Anderson-Grünesien parameter is to a very good approximation independent of temperature (Anderson, 1988). Therefore, the value calculated at reference condition is used for all T.

The dependence on temperature of the shear modulus is measured to be approximatively linear. The shear modulus at the foot of the adiabat for phase i is then computed with Eq. (A.3)

Next, each phase is compressed adiabatically from reference pressure P_0 and temperature ϑ_i to local mantle pressure and temperature (P, T). To calculate the density, the adiabat incompressibility, and the shear modulus at (P, T) we use the finite strain fourth-order Birch-Murnaghan equations of state (A.10) that we used for core materials. Unlike for the core materials, the bulk moduli and their derivatives with respect to pressure in (A.10) are not isothermal but adiabatic. Furthermore, we assume that the derivatives of the elastic moduli at (P_0, ϑ) can be approximated by their values at reference temperature (P_0, T_0).

The next step is the determination of the food of the adiabat. The food of the adiabat is different for each mineral, it is the temperature ϑ_i one would obtain by decompressing adiabatically mineral i from (P, T) to reference pressure P_0. Within the quasi-harmonic approximation (Anderson, 1979) the adiabatic temperature profile can be written as:

$$T(P, \vartheta) = \vartheta \exp \left\{ \frac{\gamma(P_0, T_0)}{q} \left[\left(\frac{\rho(P_0, T_0)}{\rho(P_0, \vartheta)} \right)^q - \left(\frac{\rho(P_0, T_0)}{\rho(P_0, T)} \right)^q \right] \right\}, \qquad (B.6)$$

where γ is the Grüneisen parameter and q is a measured constant close to 1. The foot of the adiabat for each mineral i is then obtained by solving (B.6) with

61

	ρ	ρ_{Fe}	a_0	b_0	c_0	γ_{th}	K_S	$K_{S,\text{Fe}}$	K'_S	$\frac{\partial K_S}{\partial T}$	μ	μ_{Fe}	μ'	$\frac{\partial \mu}{\partial T}$
	g/cm^3	g/cm^3	$10^{-5}/\text{K}$	$10^{-8}/\text{K}^2$	K		GPa	GPa		GPa/K	GPa	GPa		GPa/K
ol	3.222	1.182	2.832	0.758	0.	1.14	129.	0.	4.2	-0.016	81.	$-31.$	1.4	-0.014
wad	3.472	1.24	2.711	0.6885	0.5767	1.32	172.	0.	4.5	-0.016	112.	$-40.$	1.5	-0.014
ring	3.548	1.30	1.872	0.421	0.6537	1.21	185.	35.	4.1	-0.024	120.	$-28.$	1.3	-0.015
Mg-pv	4.108	1.07	1.17	1.51	0.	1.31	264.	0.	4.0	-0.015	175.	0.	1.8	-0.029
Mg-w	3.584	2.28	3.0	1.2	0.	1.45	163.	$-15.$	4.0	-0.019	130.	$-77.$	2.3	-0.024
cpl	3.208	0.80	2.86	0.72	0.	1.05	112.	$-5.$	6.6	-0.012	75.	10.	1.6	-0.012
cph	3.297	0.82	2.86	0.72	0.	1.05	112.	$-5.$	6.6	-0.012	75.	10.	1.6	-0.012
opx	3.194	0.81	2.86	0.72	0.	1.05	109.	$-5.$	7.0	-0.012	75.	10.	1.6	-0.012
cpx	3.277	0.38	2.32	1.88	0.	1.06	105.	13.	$6.2 - 1.9x_{Fe}$	-0.013	67.	$-6.$	1.7	-0.010
aki	3.810	1.1	2.27	0.682	-0.385	1.38	212.	0.	5.6	-0.017	132.	$-41.$	1.7	-0.017
gt	3.565	0.76	2.08	1.43	0.	1.17	171.	15.	4.4	-0.021	92.	7.	1.4	-0.010

Table B.12: Thermoelastic constants at STP conditions ($P = 10^5$Pa, $T = 298$K) (Verhoeven et al., 2005; Cammarano et al., 2003) for the mantle. ρ, K_S, and μ are the density, the bulk modulus, and the shear modulus. Derivatives of the moduli with respect to pressure are denoted with a "′" superscript. ρ_{Fe}, $K_{S,\text{Fe}}$, and μ_{Fe} give the iron content dependence of the density, bulk modulus and shear modulus. The coefficients a_0, b_0 and c_0 govern the expansion of the thermal expansivity: $\alpha(T) = a_0 + b_0 T - c_0 T^{-2}$. Abbreviations: see Table [B.13].

respect to ϑ_i. The numerical values of the required thermodynamic parameters are given in Tab. B.12.

In the last step we calculate the density and the elastic moduli of the mineral phase aggregate and use (A.21) and (A.22) to obtain the seismic velocities v_P and v_S at local (P,T).

olivine (ol)	$(Mg_{1-y}Fe_y)_2SiO_4$
wadsleyite (wad)	$(Mg_{1-y}Fe_y)_2SiO_4$
ringwoodite (ring)	$(Mg_{1-y}Fe_y)_2SiO_4$
Mg-perovskite (Mg-pv)	$(Mg_{1-y}Fe_y)SiO_3$
Mg-wüstite (Mg-w)	$(Mg_{1-y}Fe_y)O$
clinopyroxene LP (cpl)	$(Mg_{1-y}Fe_y)SiO_3$
clinopyroxene HP (cph)	$(Mg_{1-y}Fe_y)SiO_3$
orthopyroxene (opx)	$(Mg_{1-y}Fe_y)SiO_3$
Ca-pyroxene (cpx)	$Ca(Mg_{1-y}Fe_y)Si_2O_6$
akimotoite (aki)	$(Mg_{1-y}Fe_y)SiO_3$
garnet (gt)	$(Mg_{1-y}Fe_y)SiO_3$

Table B.13: Chemical formulas of the mineral modes and mantle high pressure phases.

References

Acuña, M. H., Connerney, J. E. P., Ness, N. F., Lin, R. P., Mitchell, D., Carlson, C. W., McFadden, J., Anderson, K. A., Reme, H., Mazelle, C., Vignes, D., Wasilewski, P., Cloutier, P., Apr. 1999. Global Distribution of Crustal Magnetization Discovered by the Mars Global Surveyor MAG/ER Experiment. Science 284, 790–793. doi: 10.1126/science.284.5415.790

Ahrens, T. J., Holland, K. G., Chen, G. Q., Apr. 2002. Phase diagram of iron, revised-core temperatures. Geophys. Res. Lett. 29, 54–1. doi: 10.1029/2001GL014350

Anderson, D. L., May 1988. Temperature and pressure derivatives of elastic constants with application to the mantle. J. Geophys. Res. 93 (B5), 4688–4700. doi: 10.1029/JB093iB05p04688

Anderson, O. L., Jul. 1979. Evidence supporting the approximation $\gamma\rho$=const for the Grüneisen parameter of the earth's lower mantle. J. Geophys. Res. 84, 3537–3542.

Anderson, O. L., Nov. 2000. The Grüneisen ratio for the last 30 years. Geophys. J. Int. 143, 279–294. doi: 10.1046/j.1365-246X.2000.01266.x

Anderson, W. W., Ahrens, T. J., Mar. 1994. An equation of state for liquid iron and implications for the Earth's core. J. Geophys. Res. 99, 4273–4284.

Andrault, D., Bolfan-Casanova, N., Ohtaka, O., Fukui, H., Arima, H., Fialin, M., Funakoshi, K., May 2009. Melting diagrams of Fe-rich alloys determined from synchrotron in situ measurements in the 15-23 GPa pressure range. Physics of the Earth and Planetary Interiors 174 (1-4), 181 – 191. doi: 10.1016/j.pepi.2008.09.020

Balog, P. S., Secco, R. A., Rubie, D. C., Frost, D. J., Feb. 2003. Equation of state of liquid $Fe - 10wt\%S$: Implications for the metallic cores of planetary bodies. J. Geophys. Res. (Solid Earth) 108. doi: 10.1029/2001JB001646

Bertka, C. M., Fei, Y., Apr. 1998. Density profile of an SNC model Martian interior and the moment-of-inertia factor of Mars. Earth Planet. Sci. Lett. 157, 79–88. doi: 10.1016/S0012-821X(98)00030-2

Boehler, R., Jul. 1992. Melting of the Fe − FeO and the Fe − FeS systems at high pressure: Constraints on core temperatures. Earth Planet. Sci. Lett. 111, 217–227. doi: 10.1016/0012-821X(92)90180-4

Boehler, R., Jun. 1993. Temperatures in the Earth's core from melting-point measurements of iron at high static pressures. Nature 363, 534–536.

Brett, R., Bell, P. M., 1969. Melting relations in the Fe-rich portion of the system Fe-FeS at 30 kb pressure. Earth Planet. Sci. Lett. 6, 479–482. doi: 10.1016/0012-821X(69)90119-8

Breuer, D., Spohn, T., Jul. 2003. Early plate tectonics versus single-plate tectonics on Mars: Evidence from magnetic field history and crust evolution. J. Geophys. Res. (Planets) 108, 8–1. doi: 10.1029/2002JE001999

Burbine, T. H., O'Brien, K. M., May 2004. Determining the possible building blocks of the Earth and Mars. Meteoritics and Planetary Science 39, 667–681.

Callen, B. H., 1985. Thermodynamics and an Introduction to Thermostatistics, second edition Edition. Wiley & Sons.

Cammarano, F., Goes, S., Vacher, P., Giardini, D., Aug. 2003. Inferring upper-mantle temperatures from seismic velocities. Phys. Earth Planet. Inter. 138, 197–222. doi: 10.1016/S0031-9201(03)00156-0

Chen, B., Li, J., Hauck, S. A. I., April 2008. Non-ideal liquidus curve in the Fe-S system and Mercury's snowing core. Geophys. Res. Lett. 35, L07201. doi: 10.1029/2008GL033311

Chudinovskikh, L., Boehler, R., May 2007. Eutectic melting in the system Fe-S to 44 GPa. Earth Planet. Sci. Lett. 257 (1-2), 97–103. doi: 10.1016/j.epsl.2007.02.024

Dahlen, F. A., Tromp, J., September 1998. Theoretical Global Seismology. Princeton University Press, Princeton, New Jersey.

Dreibus, G., Wänke, H., Jun. 1985. Mars, a volatile-rich planet. Meteoritics 20, 367–381.

Fei, Y., Li, J., Bertka, C. M., Prewitt, C. T., November 2000. Structure type and bulk modulus of Fe_3S, a new iron-sulfur compound. American Mineralogist 85 (11-12), 1830–1833.

Hastings, W. K., April 1970. Monte Carlo sampling methods using Markov chains and their applications. Biometrika 57, 97–109. doi: `10.1093/biomet/57.1.97`

Hauck, S. A., Aurnou, J. M., Dombard, A. J., Sep. 2006. Sulfur's impact on core evolution and magnetic field generation on Ganymede. J. Geophys. Res. (Planets) 111, 1–14. doi: `10.1029/2005JE002557`

Irifune, T., Nishiyama, N., Kuroda, K., Inoue, T., Isshiki, M., Utsumi, W., Funakoshi, K.-I., Urakawa, S., Uchida, T., Katsura, T., Ohtaka, O., Mar. 1998. The Postspinel Phase Boundary in Mg2SiO4 Determined by in Situ X-ray Diffraction. Science 279, 1698–1700. doi: `10.1126/science.279.5357.1698`

Ito, E., Takahashi, E., Aug. 1989. Postspinel transformations in the system $Mg_2SiO_4 - Fe_2SiO_4$ and some geophysical implications. J. Geophys. Res. (Solid Earth) 94, 10637–10646.

Kaiura, G. H., Toguri, J. M., 1979. Densities of the Molten FeS, $FeS - Cu_2S$ and $Fe - S - O$ Systems Utilizing a Bottom-Balance Archimedean Technique. Canadian Metallurgical Quarterly 18 (2), 155–164.

Khan, A., Connolly, J. A. D., July 2008. Constraining the composition and thermal state of Mars from inversion of geophysical data. J. Geophys. Res. (Planets) 113, E07003. doi: `10.1029/2007JE002996`

Konopliv, A. S., Asmar, S. W., Foiles, S. M., Karatekin, Ö., Nunes, D. C., Smrekar, S. E., Yoder, C. F., Zuber, M. T., January 2011. Mars High Resolution Gravity Fields from MRO, Mars Seasonal Gravity, and Other Dynamical Parameters. Icarus 211 (1), 401 – 428. doi: 10.1016/j.icarus.2010.10.004

Konopliv, A. S., Yoder, C. F., Standish, E. M., Yuan, D.-N., Sjogren, W. L., May 2006. A global solution for the Mars static and seasonal gravity, Mars orientation, Phobos and Deimos masses, and Mars ephemeris. Icarus 182, 23–50. doi: 10.1016/j.icarus.2005.12.025

Kuwayama, Y., Hirose, K., February 2004. Phase relations in the system Fe − FeSi at 21 GPa. American Mineralogist 89 (2-3), 273–276.

Lainey, V., Dehant, V., Pätzold, M., Apr. 2007. First numerical ephemerides of the Martian moons. Astronomy and Astrophysics 465, 1075–1084. doi: 10.1051/0004-6361:20065466

Lemoine, F. G., Bruinsma, S., Chinn, D. S., Forbes, J. M., August 2006. Thermospheric Studies with Mars Global Surveyor. American/AAS Strodynamics Conference.

Li, J., Fei, Y., Mao, H. K., Hirose, K., Shieh, S. R., Dec. 2001. Sulfur in the Earth's inner core. Earth Planet. Sci. Lett. 193, 509–514.

Lodders, K., Fegley, B., Apr. 1997. An Oxygen Isotope Model for the Composition of Mars. Icarus 126, 373–394. doi: 10.1006/icar.1996.5653

Longhi, J., Knittle, E., Holloway, J. R., Wänke, H., 1992. The bulk composition, mineralogy and internal structure of Mars. Mars, pp. 184–208.

Marty, J. C., Balmino, G., Rosenblatt, P., Duron, J., Le Maistre, S., Rivoldini, A., Dehant, V., Van Hoolst, T., March 2009. Martian gravity field model and its time variations from MGS and ODYSSEY data. Planetary and Space Science 57 (3), 350–363. doi: 10.1016/j.pss.2009.01.004

Matas, J., Bass, J., Ricard, Y., Mattern, E., Bukowinski, M. S. T., Aug. 2007. On the bulk composition of the lower mantle: predictions and limitations from generalized inversion of radial seismic profiles. Geophysical Journal International 170, 764–780. doi: 10.1111/j.1365-246X.2007.03454.x

McSween, Jr., H. Y., Nov. 1994. What we have learned about Mars from SNC meteorites. Meteoritics 29, 757–779.

Mocquet, A., Vacher, P., Grasset, O., Sotin, C., Nov. 1996. Theoretical seismic models of Mars: the importance of the iron content of the mantle. Planet. Space Sci. 44, 1251–1268.

Mohapatra, R. K., Murty, S. V. S., Feb. 2003. Precursors of Mars: Constraints from nitrogen and oxygen isotopic compositions of martian meteorites. Meteoritics and Planetary Science 38, 225–242.

Morard, G., Andrault, D., Guignot, N., Sanloup, C., Mezouar, M., Petitgirard, S., Fiquet, G., August 2008. In situ determination of $Fe - Fe_3S$ phase diagram and liquid structural properties up to 65 GPa. Earth Planet. Sci. Lett. 272 (3-4), 620–626. doi: 10.1016/j.epsl.2008.05.028

Nagamori, M., 1969. Density of molten Ag–S, Cu–S, and Ni–S systems. Trans. Metall Soc. AIME 245, 1897–1902.

Neumann, G. A., Zuber, M. T., Wieczorek, M. A., McGovern, P. J., Lemoine, F. G., Smith, D. E., Aug. 2004. Crustal structure of Mars from gravity and topography. J. Geophys. Res. (Planets) 109, E08002. doi: 10.1029/2004JE002262

Nishida, K., Terasaki, H., Ohtani, E., Suzuki, A., August 2008. The effect of sulfur content on density of the liquid Fe-S at high pressure. Physics and Chemistry of Minerals 35 (7), 417–423. doi: 10.1007/s00269-008-0236-4

Poirier, J.-P., Sep. 1994. Light elements in the Earth's outer core: A critical review. Phys. Earth Planet. Inter. 85, 319–337. doi: 10.1016/0031-9201(94)90120-1

Poirier, J.-P., Mar. 2000. Introduction to the Physics of the Earth's Interior. Introduction to the Physics of the Earth's Interior, by Jean-Paul Poirier, pp. 326. ISBN 052166313X. Cambridge, UK: Cambridge University Press, March 2000.

Rivoldini, A., Van Hoolst, T., Verhoeven, O., May 2009. The interior structure of Mercury and its core sulfur content. Icarus 201 (1), 12–30. doi: 10.1016/j.icarus.2008.12.020

Robinson, M. S., Taylor, G. J., Jun. 2001. Ferrous oxide in Mercury's crust and mantle. Meteoritics and Planetary Science 36, 841–847.

Rubie, D. C., Gessmann, C. K., Frost, D. J., May 2004. Partitioning of oxygen during core formation on the Earth and Mars. Nature 429, 58–61. doi: 10.1038/nature02473

Sanloup, C., Fei, Y., Oct. 2004. Closure of the $Fe - S - Si$ liquid miscibility gap at high pressure. Phys. Earth Planet. Inter. 147, 57–65. doi: 10.1016/j.pepi.2004.06.008

Sanloup, C., Jambon, A., Gillet, P., Mar. 1999. A simple chondritic model of Mars. Phys. Earth Planet. Inter. 112, 43–54.

Seidelmann, P. K., Abalakin, V. K., Bursa, M., Davies, M. E., de Bergh, C., Lieske, J. H., Oberst, J., Simon, J. L., Standish, E. M., Stooke, P., Thomas, P. C., Jan. 2002. Report of the IAU/IAG Working Group on Cartographic Coordinates and Rotational Elements of the Planets and Satellites: 2000. Celestial Mechanics and Dynamical Astronomy 82, 83–111.

Shen, G., Mao, H.-k., Hemley, R. J., Duffy, T. S., Rivers, M. L., February 1998. Melting and crystal structure of iron at high pressures and temperatures. Geophys. Res. Lett. 25 (3), 373–376. doi: 10.1029/97GL03776

Smith, D. E., Zuber, M. T., Torrence, M. H., Dunn, P. J., Neumann, G. A., Lemoine, F. G., Fricke, S. K., May 2009. Time variations of Mars' gravi-

69

tational field and seasonal changes in the masses of the polar ice caps. J. Geophys. Res. 114, E05002. doi: 10.1029/2008JE003267

Sohl, F., Spohn, T., Jan. 1997. The interior structure of Mars: Implications from SNC meteorites. J. Geophys. Res. 102, 1613–1636. doi: 10.1029/96JE03419

Stacey, F. D., October 1977. Applications of thermodynamics to fundamental earth physics. Geophysical Surveys 3, 175–204. doi: 10.1007/BF01449192

Stacey, F. D., Davis, P. M., 2008. Physics of the Earth. Cambridge University Press.

Stevenson, D. J., Jul. 2001. Mars' core and magnetism. Nature 412, 214–219. doi: 10.1038/35084155

Stewart, A. J., Schmidt, M. W., van Westrenen, W., Liebske, C., Jun. 2007. Mars: A New Core-Crystallization Regime. Science 316, 1323–1325. doi: 10.1126/science.1140549

Stixrude, L., Lithgow-Bertelloni, C., Aug. 2005. Thermodynamics of mantle minerals - I. Physical properties. Geophys. J. Int. 162, 610–632. doi: 10.1111/j.1365-246X.2005.02642.x

Takahashi, E., Sep. 1990. Speculations on the Archean mantle: Missing link between komatiite and depleted garnet peridotite. J. Geophys. Res. 95, 15941–15954.

Tarantola, A., January 2005. Inverse Problem Theory and Methods for Model Parameter Estimation. Society for Industrial Mathematics.

Trampert, J., Vacher, P., Vlaar, N., Aug. 2001. Sensitivities of seismic velocities to temperature, pressure and composition in the lower mantle. Phys. Earth Planet. Inter. 124, 255–267.

Tsuno, K., Ohtani, E., Terasaki, H., Jan. 2007. Immiscible two-liquid regions in the $Fe - O - S$ system at high pressure: Implications for planetary cores. Phys. Earth Planet. Inter. 160, 75–85. doi: 10.1016/j.pepi.2006.09.004

Vacher, P., Mocquet, A., Sotin, C., Apr. 1998. Computation of seismic profiles from mineral physics: the importance of the non-olivine components for explaining the 660 km depth discontinuity. Phys. Earth Planet. Inter. 106, 275–298.

Van Hoolst, T., Dehant, V., Roosbeek, F., Lognonné, P., Feb. 2003. Tidally induced surface displacements, external potential variations, and gravity variations on Mars. Icarus 161, 281–296. doi: `10.1016/S0019-1035(02)00045-3`

Van Hoolst, T., Jacobs, C., Nov. 2003. Mercury's tides and interior structure. J. Geophys. Res. (Planets) 108 (E11). doi: `10.1029/2003JE002126`

van Thienen, P., Rivoldini, A., Van Hoolst, T., Lognonné, P., Nov. 2006. A top-down origin for martian mantle plumes. Icarus 185, 197–210. doi: `10.1016/j.icarus.2006.06.008`

Verhoeven, O., Mocquet, A., Vacher, P., Rivoldini, A., Menvielle, M., Arrial, P.-A., Choblet, G., Tarits, P., Dehant, V., Van Hoolst, T., March 2009. Constraints on thermal state and composition of the Earth's lower mantle from electromagnetic impedances and seismic data. J. Geophys. Res. (Solid Earth) 114, B03302. doi: `10.1029/2008JB005678`

Verhoeven, O., Rivoldini, A., Vacher, P., Mocquet, A., Choblet, G., Menvielle, M., Dehant, V., Van Hoolst, T., Sleewaegen, J., Barriot, J.-P., Lognonné, P., Apr. 2005. Interior structure of terrestrial planets: Modeling Mars' mantle and its electromagnetic, geodetic, and seismic properties. J. Geophys. Res. (Planets) 110 (E9). doi: `10.1029/2004JE002271`

Wieczorek, M. A., Zuber, M. T., Jan. 2004. Thickness of the Martian crust: Improved constraints from geoid-to-topography ratios. J. Geophys. Res. (Planets) 109 (E18), E01009. doi: `10.1029/2003JE002153`

Yoder, C. F., Konopliv, A. S., Yuan, D. N., Standish, E. M., Folkner, W. M., Apr. 2003. Fluid Core Size of Mars from Detection of the Solar Tide. Science 300, 299–303. doi: `10.1126/science.1079645`

Zhang, L., Fei, Y., April 2008. Effect of Ni on Fe − FeS phase relations at high pressure and high temperature. Earth Planet. Sci. Lett. 268 (1-2), 212–218. doi: 10.1016/j.epsl.2008.01.028

Zharkov, V. N., Gudkova, T. V., Dec. 1999. Interior structure models, Fe/Si ratio and parameters of figure for Mars. Phys. Earth Planet. Inter. 117, 407–420.

Zharkov, V. N., Gudkova, T. V., Sep. 2005. Construction of Martian Interior Model. Solar System Research 39, 343–373. doi: 10.1007/s11208-005-0049-7

Zharkov, V. N., Gudkova, T. V., Molodensky, S. M., 2009. On models of Mars' interior and amplitudes of forced nutations: 1. The effects of deviation of Mars from its equilibrium state on the flattening of the core-mantle boundary. Physics of the Earth and Planetary Interiors 172 (3-4), 324–334.

Zuber, M. T., Jul. 2001. The crust and mantle of Mars. Nature 412, 220–227. doi: 10.1038/35084163

>Geodesy data constraint the interior structure and composition of Mars. >Geodesy data imply that Mars has no inner core. >The radius of the liquid core is 179465km. >The core sulfur concentration is 162wt% if sulfur is the only light element in the core. >Interior structure models with a chondritic Fe/Si ratio are consistent with the data.